



20 Furthermore, thermo-mechanics within representative volumes enclosing unit as well as mortar  
21 and their correlation with the global thermo-mechanical response is studied. Such 2-D micro-  
22 scale thermo-mechanical computations on masonry walls followed by a detailed discussion on  
23 their thermo-mechanics are one of the novel features of the present study. It is observed that  
24 thermal bowing resulted from a complex interaction between thermal dilation and cracking and  
25 crushing in the mortar and unit within the masonry structure.

26 **Keywords:** Thermo-mechanical analysis, Masonry, Fire resistance, Nonlinear thermal gradients.

## 27 **1 Introduction**

28 Ancient and modern infrastructural utilities employ masonry as one of the predominant material  
29 for structural and/or non-structural elements attributing to its excellent thermal, mechanical and  
30 acoustic properties. The response of such masonry structures has been well studied in the context  
31 of static and dynamic loading scenarios [1,2]. However, limited rather scarce understanding is  
32 available in the literature in the context of masonry structures subjected to fire exposure [3]. The  
33 design of masonry structures subjected to fire is usually done by the fire resistance rating  
34 quantification, which is essentially the time required by the structure for attaining the prescribed  
35 failure limit state which is usually in terms of strength, integrity and deflection limits [4]. The  
36 fire resistance ratings of masonry structures are normally evaluated by a) experimental methods  
37 [3], b) codified approaches (e.g. EN 1996-1-2 [4] and ACI 216.1-07 [5]) and c) numerical  
38 models (e.g. [6,7]).

39 Experimental methods involve the fire resistance rating quantification by exposing the  
40 masonry structure to a given fire scenario. The early experimental investigations on masonry  
41 subjected to fire include the full-scale fire tests on clay brick masonry walls conducted at the  
42 Experimental building station, Australia [8] to study the phenomenon of fire-induced thermal

43 bowing. Lawrence and Gnanakrishnan [9] conducted a comprehensive experimental  
44 investigation on clay brick masonry walls subjected to fire and quantified the effects of  
45 slenderness ratio and applied axial load on the overall thermo-mechanical behavior. Shields et al.  
46 [10] investigated the thermo-mechanical response of masonry walls subjected to the BS-476 fire  
47 exposure. Lavery et al. [11] tested scaled concrete brick masonry walls subjected to various  
48 load levels and fire exposures and had explained the phenomena of thermal bowing and reverse  
49 thermal bowing. Recently, Nguyen and Meftah [12] experimentally investigated the thermo-  
50 mechanical response of hollow clay block masonry walls subjected to fire exposure, and spalling  
51 was observed in their experimental investigation. Although such full-scale tests facilitate precise  
52 understanding of the thermo-mechanics of the masonry walls, they cannot be performed  
53 regularly for the prescriptive and/or performance based design of masonry walls subjected to fire  
54 due to the explicit costs and time involved in such tests.

55 Codified approaches essentially involve fire resistance rating quantification of masonry walls  
56 from the tabulated data available in the building codes (e.g. EN 1996-1-2 [13], IS-1642 [14] and  
57 ACI 216.1-07 [5]) as a function of the wall thickness. However, such an approach is prescriptive  
58 in nature and does not account for critical phenomena which may significantly influence the  
59 thermo-mechanics of the masonry wall like load level, geometric effects, boundary conditions  
60 and realistic fire exposures. These limitations can be alleviated with the aid of experimentally  
61 validated numerical models. Very limited numerical investigations have been performed on the  
62 numerical simulation of the thermo-mechanical response of the masonry structures subjected to  
63 fire. An early numerical model developed in this context includes the 2-D finite element (FE)  
64 model developed by Dhansekaran et al. [6]. Their FE model demonstrated thermal bowing in  
65 masonry walls and it is essentially a layered shell element which performs time-variant

66 mechanical analysis with thermal gradients and temperature-dependent mechanical properties as  
67 input. Nadjai et al. [15] developed a 2-D FE based micro model for nonlinear thermo-mechanical  
68 analysis of masonry walls and successfully implemented in MasSET programme [16]. Their 2-D  
69 FE model accounts for geometric and material nonlinearities, thermal gradients, temperature-  
70 dependent material properties and transient states of strain. Later, they had demonstrated  
71 applications pertaining to the behavior of compartmental masonry walls subjected to fire  
72 exposure [17] using their MasSET programme. Nguyen and Meftah [18] demonstrated a  
73 numerical validation study on a hollow clay block masonry subjected to fire exposure utilizing a  
74 nonlinear 3-D FE micro modelling approach in Cast3M. To model the observed spalling in the  
75 experiment, their numerical model considered a crushing-detachment-buckling based spalling  
76 criteria and was successfully validated against the experimental observations. Recently, Kumar  
77 and Srivastava [19] had demonstrated the effect of masonry infill on the in-plane and out of  
78 plane response of the fire exposed masonry in-filled reinforced concrete frame utilizing a  
79 nonlinear 3-D FE simplified micro model in ANSYS. Their numerical investigation indicated a  
80 significant influence of masonry on the overall stability of the masonry in-filled RC frame at  
81 elevated temperatures.

82       Aforementioned works pertaining to the numerical modelling of masonry structures provide a  
83 perspective on the thermo-mechanical response of masonry walls subjected to fire. However,  
84 masonry being a complex material with different thermal and mechanical properties of the  
85 constituents, a detailed understanding is needed on the unit level thermo-mechanics and its  
86 correlation with the global thermo-mechanical response. Such a discussion is observed to be  
87 missing in the present literature and is the prime focus of the present study. This study  
88 demonstrates an intricate numerical investigation on masonry walls subjected to fire utilizing a

89 2-D FE micro model in DIANA-FEA [20]. The unit and mortar are modelled separately within  
90 the 2-D FE model and it accounts for a) geometric and material nonlinearities, b) nonlinear  
91 thermal gradients, c) temperature-dependent mechanical and thermal properties, d) cracking and  
92 crushing of materials, and e) transient states of strain.

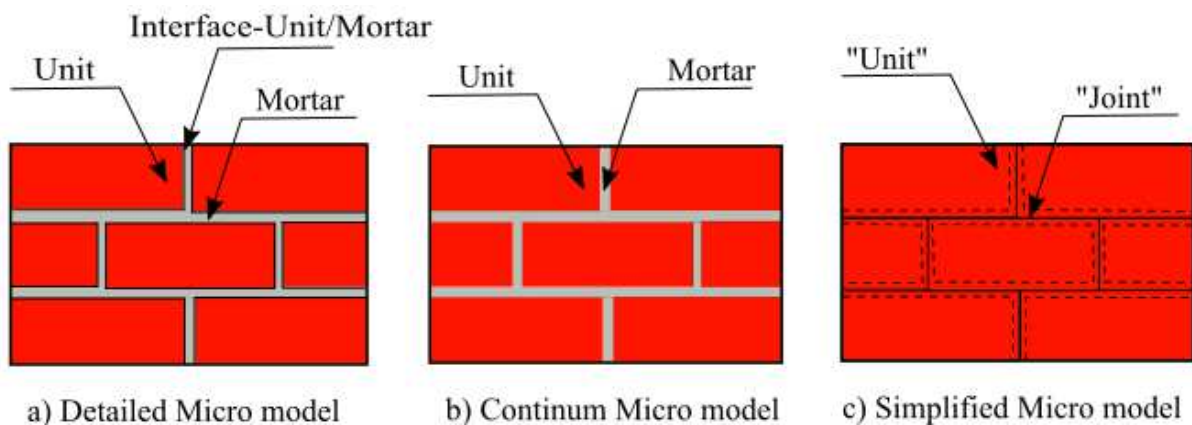
93 The present paper is organized as follows. Section 2 presents the theoretical aspects of the 2-D  
94 FE modelling based simulation framework which include assumptions, thermo-mechanical  
95 components of the FE model, and temperature-dependent material models. Next, Section 3  
96 presents the experimental validation study pertaining to half-scale masonry wall subjected to fire  
97 exposure. Section 4 demonstrates a scenario based thermo-mechanical analysis of full-scale  
98 masonry wall subjected to fire exposure. Finally, Section 5 concludes the present study.

## 99 **2 Simulation framework**

100 **This study utilizes a nonlinear 2-D FE micro modelling based framework to evaluate the thermo**  
101 **mechanical behaviour of solid brick masonry walls subjected to fire.** The framework is  
102 formulated in a plane stress setting assuming a uniform fire exposure and mechanical boundary  
103 conditions along the top and bottom surfaces of the wall. In the case of thermal analysis, such an  
104 approach is considered ideal as no lateral conduction is expected for such a uniform fire  
105 exposure. However, in the case of mechanical analysis such plane stress approach may not be  
106 ideal in case of walls with complete or partial lateral restraint (in the direction perpendicular to  
107 the 2D simulation plane). Moreover, the unit-joint thermo-mechanical interactions along the  
108 lateral direction are ignored. Such a 2-D framework with above mentioned plane stress  
109 idealization facilitates computationally efficient thermo-mechanical analysis of masonry walls  
110 subjected to fire. However, in scenarios involving a deviation of the aforementioned assumption,

111 3-D FE modelling should be preferred. Furthermore, the developed framework in its present  
112 form is not applicable for the thermo-mechanical analysis of hollow-brick masonry walls.

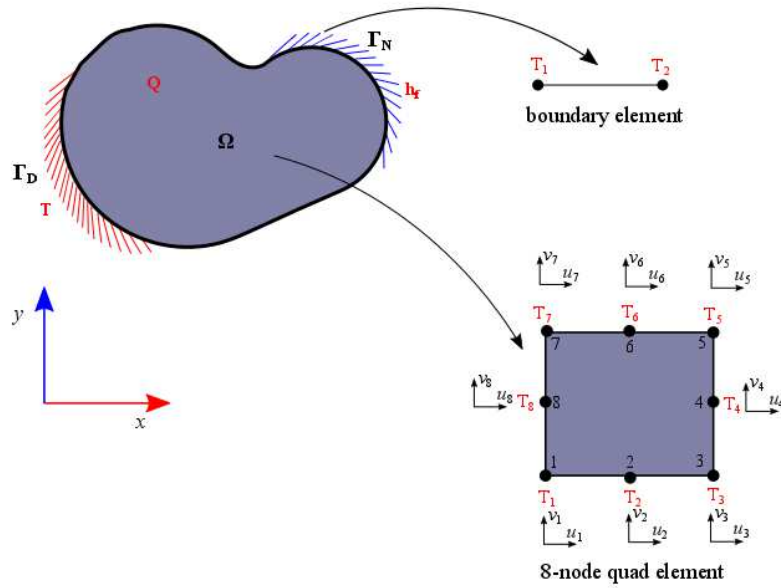
113 It is to be noted that FE based computational modelling of masonry is usually done utilizing  
114 micro and macro based modelling strategies, respectively [2]. Within the micro modelling, which  
115 is the main focus of the present study, three approaches are possible, namely: a) detailed micro  
116 modelling, b) continuum micro modelling, and c) simplified micro modelling (Figure 1). In the  
117 case of detailed micro modelling, the unit, mortar and the unit-mortar interface are modelled  
118 separately. Continuum micro modelling is a simplified version of detailed micro modelling  
119 strategy, with bonded interfaces. In the case of simplified micro modelling strategy, unit and  
120 mortar are modelled together as a composite unit with interface elements at the half thickness of  
121 the mortar. These approaches have their own merits and de-merits and have been a matter of  
122 discussion among various researchers (e.g. Lourenço [2] and Mohyeddin [21] ). In the context of  
123 thermo-mechanical modelling of masonry exposed to fire, detailed micro modelling strategy  
124 facilitates precise modelling of physical phenomena and is capable of considering localized  
125 failure modes (cracking, crushing and various modes of fracture at the unit-mortar interface).



127 **Figure 1: Micro modelling strategies in masonry [2].**

128 However, at elevated temperatures, the temperature-dependent mechanical behavior of the unit-  
129 mortar interface is still not established due to the lack of comprehensive experimental research,  
130 specifically targeted to the temperature-dependency of the nonlinear interface behavior. This  
131 limitation can be partly alleviated by extending the temperature-dependency in mechanical  
132 properties of cement mortar to the unit-mortar interface. However, detailed model calibration  
133 studies are required to account for the lack of experimental data pertaining to the temperature-  
134 dependent coupled tension-shear failure mode in cement mortar [22] . Furthermore, convergence  
135 issues are expected due to the complex temperature-dependent interface nonlinearity. In view of  
136 such complex limitations, the present study models unit and mortar separately in a combined  
137 geometric and material nonlinearity setting using the continuum micro modelling strategy.  
138 Although such approach does not account for temperature-dependent interface behaviour, it  
139 accounts for the localized failures expected in the mortar joints as well as units and such  
140 approach has been successfully implemented in the past as well (e.g. [15,18]). Utilizing the  
141 aforementioned modelling strategy in the considered framework, the thermo-mechanical  
142 response histories of masonry walls are demonstrated in the present study.

143 Figure 2 shows the 2-D FE model which performs thermo-mechanical analysis with various  
144 thermal and mechanical boundary conditions. The thermo-mechanical analysis is performed  
145 utilizing a staggered one-way coupling scheme. In such a scheme, the thermal analysis is  
146 performed first on a fixed geometry followed by time-variant mechanical analysis at constant  
147 temperatures corresponding to various time steps [23]. Such a scheme is computationally  
148 efficient unlike the theoretically precise monolithic schemes [23] which might lead to a large  
149 system of equations with asymmetry and eventually makes the analysis computationally very  
150 intensive.



151

152

**Figure 2: 2-D Thermo-mechanical modelling and discretization strategy.**

153

In the context of the present simulation framework, the need for a fully coupled strategy has been

154

demonstrated to be of relatively small importance, hence the staggered analysis strategy is

155

chosen. The theoretical aspects of the individual thermal and mechanical FE models are

156

discussed in Sections 2.1 and 2.2 respectively.

157

## 2.1 Thermal FE model

158

For a 2-D body as shown in Figure 2, the heat transfer is governed by conduction, convection

159

and radiation. Within the 2-D solid body enclosed by  $\Omega$ , heat transfer is governed by thermal

160

conduction, whereas the heat transfer from the heating source to the exposed boundaries is

161

governed by convection and radiation. The governing equation to model the heat transfer is

162

deduced from the law of energy balance and is given by

163

$$(\rho c)_T \frac{\partial T}{\partial t} = \nabla \cdot (\gamma_T \nabla T), \quad (1)$$



164 where  $(\rho c)_T$  represents temperature-dependent specific heat capacity,  $T$  represents temperature,  
 165  $\gamma_T$  represents temperature-dependent thermal conductivity tensor. It is to be noted that the  
 166 external fire temperature is applied either as Dirichlet or Neuman boundary condition  
 167 (convection and radiation). The governing equations for the convection and radiation on the  
 168 boundary  $\Gamma_N$  are given by

$$\begin{aligned}
 & (\gamma \nabla T) \cdot \mathbf{n} = -h_c (T - T_f), \\
 & (\gamma \nabla T) \cdot \mathbf{n} = -h_r \left[ (T + 273.15)^4 - (T_f + 273.15)^4 \right],
 \end{aligned} \tag{1}$$

170 where  $T_f$  represents the fire temperature,  $h_c$  represents the convective heat transfer coefficient,  
 171  $h_r$  ( $h_r = \chi \zeta \xi$ ) represents the radiative heat transfer coefficient,  $\chi$  represents the form factor,  $\zeta$   
 172 represents the emissivity, and  $\xi$  represents the Stefan-Boltzmann constant ( $5.678 \times 10^{-8} \text{W/m}^2 \text{K}^4$ ).  
 173 Ritz-Galerkin FE discretization is applied to Equation (1) utilizing the eight-node quad element  
 174 and two-node line element as shown in Figure 2. The eight-node quad element work on the solid  
 175 body enclosed by  $\Omega$ , and with four integration points in a full integration setting. Whereas the  
 176 two-node line element work on the boundary convection and radiation at the  $\Gamma_N$ , and with two  
 177 integration points in a full integration setting. Upon discretization, a system of equations is  
 178 obtained as [24]

$$\mathbf{M} \dot{\mathbf{T}}(t) + \mathbf{K} \mathbf{T}(t) = \boldsymbol{\psi}(t), \tag{2}$$

180 where  $\mathbf{M}$  represents the heat capacity matrix,  $\mathbf{K}$  represents the conductivity matrix and  $\boldsymbol{\psi}(t)$   
 181 represents the heat load vector. These systems of equations are highly nonlinear in nature due to  
 182 temperature-dependent material properties and boundary conditions and are solved iteratively

183 using the Newton-Raphson method until the  $L_2$  norm of temperature reaches the prescribed value  
184 of tolerance.

## 185 **2.2 Mechanical FE model**

186 For the 2-D FE model as shown in Figure 2, the time-variant mechanical analysis component is  
187 executed in a one-way coupling scheme, with the temperature history of the previously executed  
188 thermal analysis as an input. For the 2-D body enclosed by  $\Omega$ , the Galerkin FE discretization is  
189 applied using 8-node quad element with four integration points in a full integration setting.  
190 Subsequently, the incremental equilibrium equations are obtained as

$$191 \quad \mathbf{K}\Delta\mathbf{d} = \Delta\mathbf{F}_m + \Delta\mathbf{F}_{th}, \quad (3)$$

192 where  $\mathbf{K}$  represents the temperature-dependent element stiffness matrix derived in a total  
193 Lagrangian based formulation,  $\Delta\mathbf{d}$  represents the element displacement vector,  $\Delta\mathbf{F}_m$  represents  
194 the incremental force vector pertaining to mechanical loading, and  $\Delta\mathbf{F}_{th}$  represents the  
195 incremental force vector pertaining to thermal effects. The incremental system of equations  
196 shown in Equation (4) are derived from the principle of virtual work [24] in conjunction with  
197 temperature-dependent constitutive relation ( $\boldsymbol{\sigma} = \mathbf{D}_T(\boldsymbol{\varepsilon} - \boldsymbol{\varepsilon}_T)$ ). Wherein,  $\boldsymbol{\sigma}$  represents the second  
198 Piola-Kirchhoff tensor,  $\mathbf{D}_T$  represents the temperature-dependent constitutive matrix,  $\boldsymbol{\varepsilon}$   
199 represents the total Green-Lagrange strain,  $\boldsymbol{\varepsilon}_T$  represents the total thermal strain. A detailed  
200 description of the strain components and the constitutive matrix will be discussed subsequently.  
201 Equation (4) is highly nonlinear in nature and is solved iteratively. In the present study, the  
202 Newton-Raphson based nonlinear solution strategy is followed with a prescribed tolerance value  
203 of 0.001 on the  $L_2$  norms of energy.

### 204 2.3 Material models

205 This section illustrates the temperature-dependent material models used within the 2-D FE  
206 modelling based simulation framework. In the context of thermal analysis, the temperature-  
207 dependency in  $(\rho c)_T$  and  $\gamma_T$  in the context of thermo-mechanical modelling of masonry walls will  
208 be discussed in the respective numerical simulation sections, respectively. The total Green-  
209 Lagrange strain ( $\boldsymbol{\varepsilon}$ ) discussed in Section 2.2 is decomposed as

$$\begin{aligned} \boldsymbol{\varepsilon} &= \boldsymbol{\varepsilon}_m + \boldsymbol{\varepsilon}_T, \\ \boldsymbol{\varepsilon}_T &= \boldsymbol{\varepsilon}_{th} + \boldsymbol{\varepsilon}_{tc}, \end{aligned} \quad (4)$$

211 where  $\boldsymbol{\varepsilon}_m$ ,  $\boldsymbol{\varepsilon}_{th}$  and  $\boldsymbol{\varepsilon}_{tc}$  represent mechanical strain, total thermal strain, thermal strain and transient  
212 creep strains, respectively. A perspective on the additive decomposition of concrete strains under  
213 transient thermal conditions can be seen in [25,26]. The thermal strain is computed as

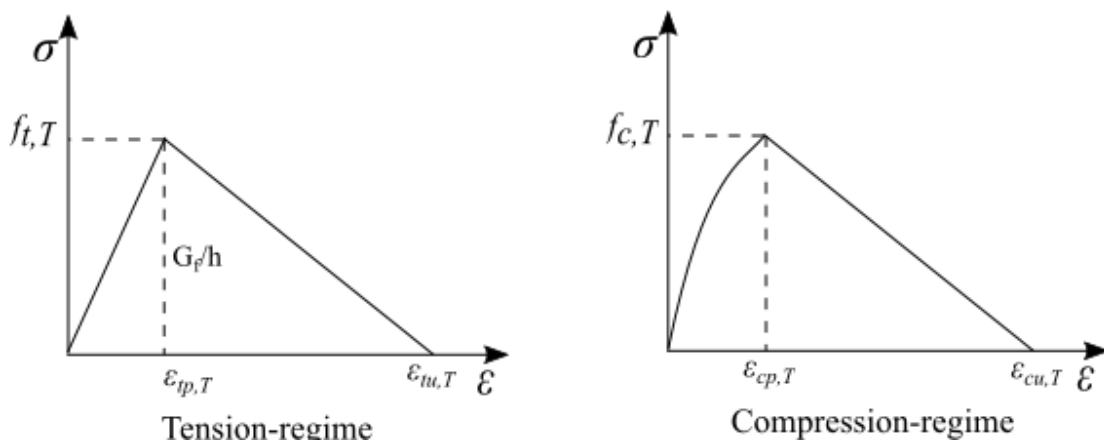
$$\boldsymbol{\varepsilon}_{th} = \alpha_T \Delta T, \quad (5)$$

215 where  $\alpha_T$  is the temperature-dependent coefficient of thermal expansion. The transient creep  
216 strain in the present FE model, the transient creep strain is modelled using the empirical  
217 relationship proposed by Anderberg and Thelanderson [27] as

$$\Delta \boldsymbol{\varepsilon}_{tc} = \tau \left( \frac{\sigma}{f_{c,20}} \right) \Delta \boldsymbol{\varepsilon}_{th}, \quad (6)$$

219 where  $\sigma$  represents stress at a given time,  $f_{c,20}$  represents the compressive strength of concrete  
220 at 20 °C and  $\tau$  is constant which ranges between 1.8 and 2.5. Further, details of the transient  
221 creep strain in the context of the present study will be explained in the respective numerical  
222 simulation sections. It is to be noted that the standard creep is not considered in combination

223 with the transient creep in the simulation framework, as the considered time scales are very small  
 224 eventually resulting negligible contribution from the standard creep [27]. The mechanical strain  
 225 is governed by the temperature-dependent constitutive relation ( $\boldsymbol{\sigma} = \mathbf{D}_T (\boldsymbol{\varepsilon} - \boldsymbol{\varepsilon}_T)$ ) and is computed  
 226 using the total strain rotating crack model. Consideration of rotating crack model instead of a  
 227 fixed crack model has been a matter of discussion among various researchers after it was first  
 228 introduced by Cope et al. [28]. In the fixed crack model, the material axes of symmetry are fixed  
 229 throughout the analysis and it may result in inaccurate model predictions in scenarios involving a  
 230 change in the principal directions during the course of loading [29]. This limitation has been  
 231 circumvented with the aid of rotating crack model, where the misalignment between the principal  
 232 directions and principal axes of symmetry is adjusted by co-rotating the principal axes of  
 233 symmetry. In a total strain rotating crack model based constitutive framework, the temperature-  
 234 dependent constitutive matrix ( $\mathbf{D}_T$ ) is computed from the 1-D temperature-dependent inelastic  
 235 constitutive relations (Figure 3) in the tensile and compressive regimes, respectively. The  
 236 background theory for such numerical implementation can be seen in [28,30] and not repeated  
 237 here for the sake of brevity.



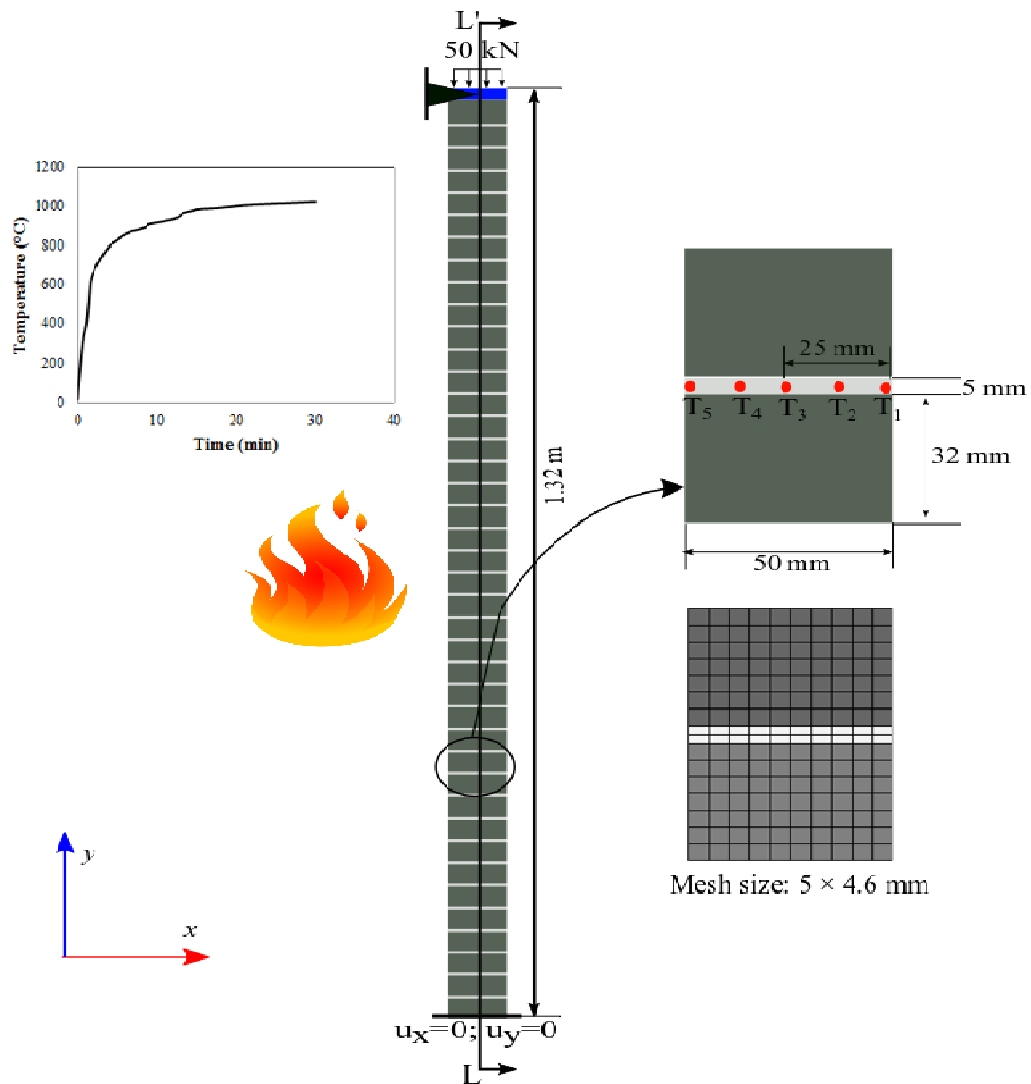
239 **Figure 3: 1-D tension and compression constitutive behavior used in the total-strain**  
240 **rotating crack model.**

241 In case of tension regime, the 1-D inelastic constitutive relation is elastic with linear softening as  
242 shown in Figure 3 and is characterized by the temperature-dependent tensile strength ( $f_{t,T}$ ) and  
243 fracture energy corresponding to mode-1 ( $G_{f1,T}$ ). The temperature dependency of above  
244 mentioned parameters in the context of the present study will be discussed in the respective  
245 numerical simulation studies. In the case of compression regime, a parabolic curve with linear  
246 softening as in EN1992-1-2 [31] is considered for 1-D inelastic constitutive relation and is  
247 characterized by temperature-dependent compressive strength ( $f_{c,T}$ ), strain at peak compressive  
248 strength ( $\epsilon_{cp,T}$ ) and ultimate compressive strain ( $\epsilon_{cu,T}$ ).

249 **3 Simulation of the experiment of half-scale masonry subjected to fire**  
250

251 The accuracy of the 2-D FE based simulation framework is established by validating the  
252 experimental investigation of Lavery et al. [11]. Their experimental study essentially involves a  
253 half-scale masonry wall (b=430 mm; h=1330 mm; t=50 mm) subjected to one-sided fire  
254 exposure as shown in Figure 4. The half-scale wall is built with concrete bricks (100×32×50  
255 mm) with 20 MPa compressive strength, bedded on **1:3 cement-sand mortar mix** (5 mm thick)  
256 pertaining to ordinary Portland cement. The wall is rested on a firm steel base and an axial load  
257 of 50 kN, which is 50% of the design ultimate load is applied on the wall through the steel plate,  
258 which is restrained against lateral translation as shown in Figure 4. The temperatures were  
259 measured at the central vertical third positions (h/3 and 2h/3) of the wall at various depths (0, t/6,  
260 t/2, 5t/6 and t) along the cross-section, whereas the lateral deflections were measured at the mid-

261 span, top and bottom, respectively. Utilizing the simulation framework, thermo-mechanical  
 262 analysis is performed with the mesh-size shown in Figure 4. The chosen mesh size is based on  
 263 mesh convergence studies.



264

265

**Figure 4: Half-scaled masonry wall subjected to fire.**

266

To quantify the effect of temperature-dependent material nonlinearity, the analysis is also

267

performed in a thermo-elastic setting with temperature-dependent thermal and mechanical

268

properties. It is to be noted that in the present simulation framework, geometric effects which

269 include large deformations, large rotations and large strains are modelled by the total Lagrangian  
 270 formulation (TLF) [32]. To quantify the effect of large strains, additional thermo-mechanical  
 271 analysis is performed without considering the geometric effects. The wall is fixed at the base and  
 272 restrained against lateral translation at the top as shown in Figure 4. The mechanical load is  
 273 applied with the aid of a steel plate, and such loading is simulated by modelling steel plate  
 274 separately with a line interface between steel plate and wall ( $K_n= 56 \text{ kN/m}^3$ ;  $K_t =5.6 \text{ kN/m}^3$ ) and  
 275 the tensile strength of the interface is taken as zero. Such values are chosen from the elastic  
 276 material properties of the steel plate in conjunction with the mesh characteristics.

### 277 3.1 Material properties

278 The material properties utilized for validating the aforementioned experimental investigation in  
 279 the context of present 2-D FE framework is presented herein. A summary of these properties at  
 280 room temperature ( $T=20 \text{ }^\circ\text{C}$ ) is shown in Table 1.

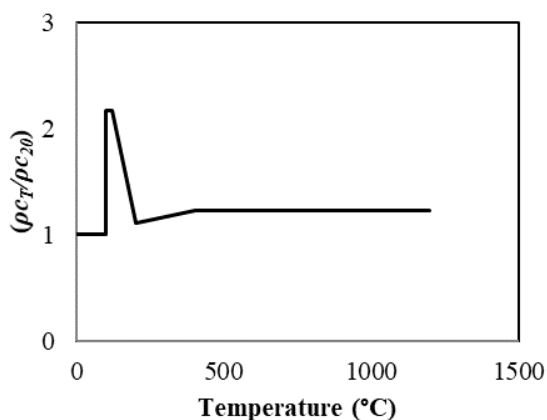
281 **Table 1: Physical properties of half-scale masonry wall subjected to fire ( $T= 20 \text{ }^\circ\text{C}$ ).**

Physical property	Value
Geometry	See Figure 4
Applied load (kN)	50
<b>Concrete unit:</b>	
Compressive strength (MPa)	20
Tensile strength (MPa)	2
Poisson's ratio	0.17
$\epsilon_{cp,20}$	0.0023
$\epsilon_{cu,20}$	0.005
Thermal expansion coefficient ( $1/^\circ\text{C}$ )	$6 \times 10^{-6}$ (Calcareous aggregates)
Heat capacity ( $\text{kJ/m}^3\text{K}$ )	2100
Thermal Conductivity ( $\text{W/mK}$ )	1.36
<b>Mortar joint:</b>	
Compressive strength (MPa)	10
Tensile strength (MPa)	1
Poisson's ratio	0.2
$\epsilon_{cp,20}$	0.004

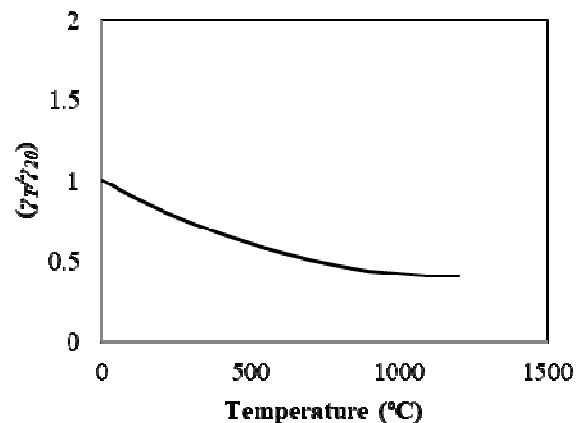
$\epsilon_{cu,20}$	0.009
Thermal expansion coefficient ( $1/^\circ\text{C}$ )	$6 \times 10^{-6}$ (Calcareous aggregates)
Heat capacity ( $\text{kJ/m}^3\text{K}$ )	2100
Thermal Conductivity ( $\text{W/mK}$ )	1.36

282

283 The temperature-dependency in specific heat capacity and thermal conductivities of concrete unit  
 284 and cement mortar are taken from the EN1992-1-2 [31] and are shown in Figure 5. It should be  
 285 noted that there is no specific mention of aforementioned thermal properties in the experimental  
 286 investigation of Lavery et al [11]. The properties from EN1992-1-2 [31] have been chosen as  
 287 they explicitly account for the latent heat effects pertaining to the inherent moisture within the  
 288 masonry wall. A moisture content of 3% by weight is assumed in the present validation study. As  
 289 will be shown subsequently, the chosen thermal properties resulted in reasonably accurate  
 290 thermal histories. The temperature-dependent thermal expansion coefficient for concrete unit as  
 291 well as cement mortar are taken from the EN1992-1-2 [31] corresponding to that of calcareous  
 292 aggregates.



a) Specific-heat capacity



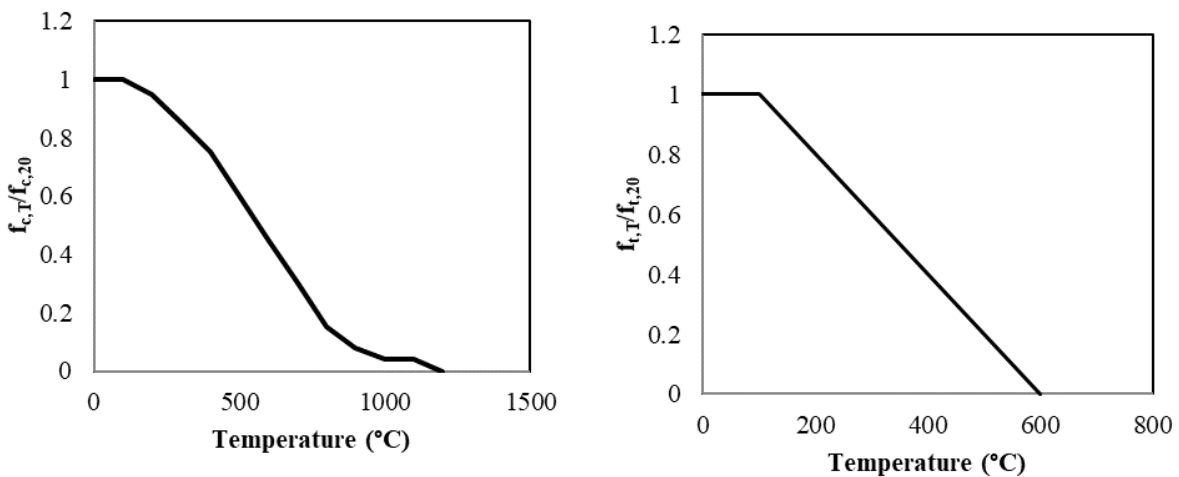
b) Thermal-conductivity



293 **Figure 5: Temperature-dependent thermal properties of concrete unit and cement mortar.**

294 The coefficient  $\tau$  pertaining to the transient creep strain is taken as 2.0 for both concrete unit and  
 295 cement mortar, and such value has been ascertained from the parametric studies. The required  
 296 material properties pertaining to the rotating crack constitutive framework discussed in Section  
 297 2.3, at  $T=20\text{ }^\circ\text{C}$  are taken from the studies of Laverty et al. [11,15]. It is to be noted that the  
 298 temperature-dependency in aforementioned mechanical properties is taken from EN1992-1-2  
 299 [31]. This is attributed to their predominate applications by the fire engineering community as  
 300 well as the lack of comprehensive experimental investigation pertaining to the constituent  
 301 materials of the half-scale test. The temperature-dependency in compressive and tensile  
 302 strengths of concrete unit and cement mortar is shown in Figure 6. The temperature-dependency  
 303 in  $\varepsilon_{cp,T}$  and  $\varepsilon_{cu,T}$  of concrete unit and cement mortar is shown in Figure 7. Further, the  
 304 temperature-dependent mode-1 fracture energy of concrete unit and cement mortar are computed  
 305 from the empirical relation provided by FIB model code [33], which is written as

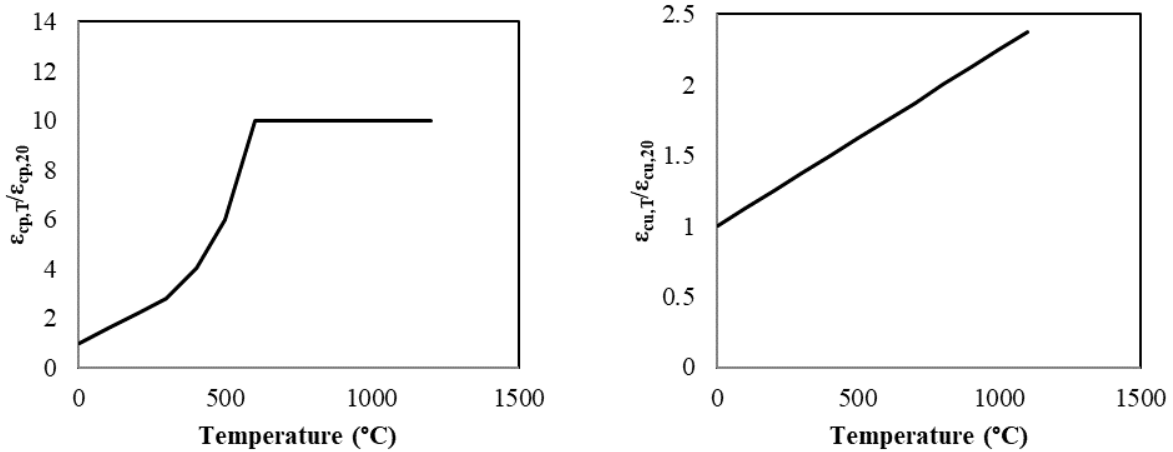
306 
$$G_{f1} = 73f_c^{0.18}. \quad (7)$$



a) Compressive strength ( $f_{c,T}$ )

b) Tensile strength ( $f_{t,T}$ )

307 **Figure 6: Temperature-dependent compressive and tensile strengths of concrete unit and**  
308 **cement mortar.**



a) Strain at peak compressive strength ( $\epsilon_{cp,T}$ )

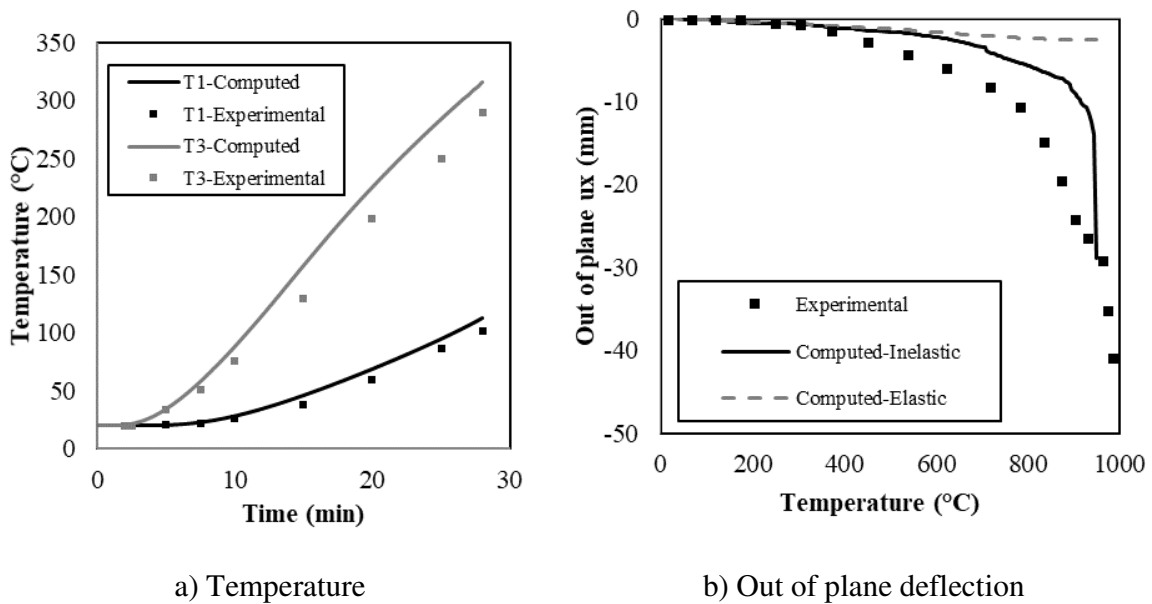
b) Ultimate compressive strain ( $\epsilon_{cu,T}$ )

309 **Figure 7: Temperature-dependent  $\epsilon_{cp,T}$  and  $\epsilon_{cu,T}$  of concrete unit and cement mortar.**

### 310 3.2 Results and discussion

311 A comparison of thermal and mechanical (out of plane deflection) response histories of the half-  
312 scale masonry wall is shown in Figure 8, for both the elastic and inelastic cases. The temperature  
313 histories at the designated locations shown in Figure 4 are in good agreement with their  
314 experimental counterparts with maximum error of 3.14%. The mechanical deflection history is  
315 in reasonably good agreement with the experimentally observed values with failure time  
316 corresponding to 23 min (numerical failure), whereas the experimentally observed failure time is  
317 28 min. The elastic mechanical response history is imprecise in comparison to the experimentally  
318 observed values, although it demonstrates thermal bowing. The effect of geometric nonlinearity  
319 on the thermo-mechanical response history is shown in Figure 9. It is observed that the

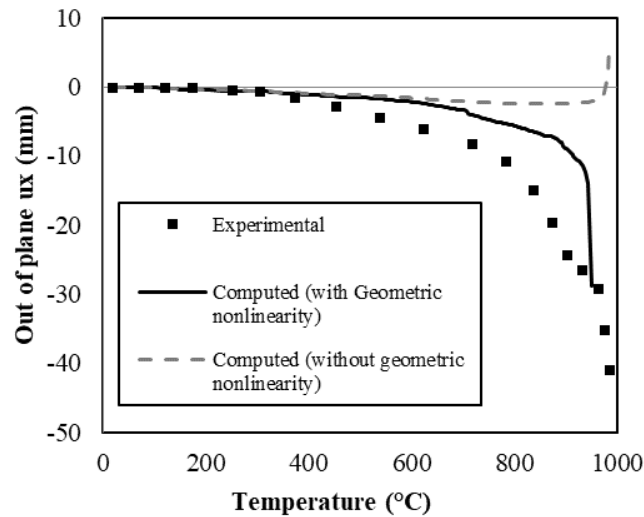
320 mechanical (out of plane deflection) response history is inaccurate with reference to the  
 321 experimentally observed values, when the geometric effects are not considered. Also, reverse  
 322 thermal bowing is observed unlike in the experiment as well as the geometric nonlinear  
 323 simulation, which is due to the temperature-dependent material degradation and damage.  
 324 Furthermore, the results indicate the importance of consideration of geometric effects in the  
 325 purview of present simulation framework. The mechanical response history of the central line of  
 326 the wall is shown in Figure 10. This response indicates thermal-bowing of the wall and its  
 327 amplification at the verge of failure. The response of masonry wall subjected to fire is governed  
 328 by the combined effects of nonlinear thermal gradients, geometric effects, applied load,  
 329 boundary conditions and temperature-dependent material degradation.



330 **Figure 8: Comparison of experimental and computed response.**

331 A discussion on these phenomena in the context of the masonry wall under consideration and  
 332 their contribution to the mechanical response history is explained herein. Figure 11 and Figure

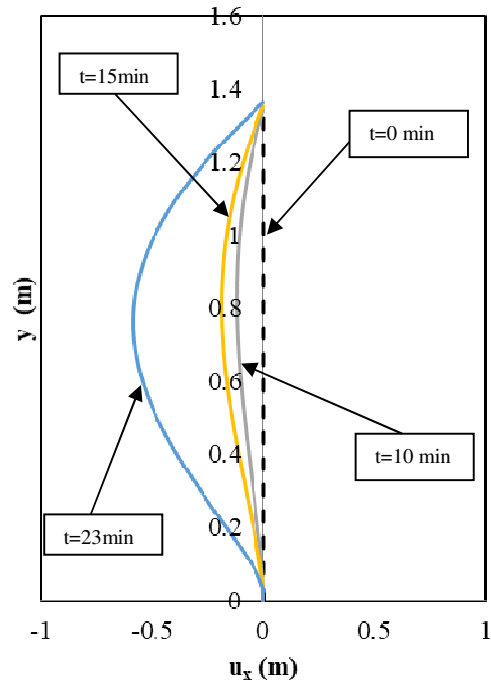
333 12, show the thermo-mechanical response of the wall under consideration at  $t=5$  min and  $t=23$   
334 min, respectively.



335

336 **Figure 9: Effect of geometric nonlinearity on the thermo-mechanical response of the half-**  
337 **scale wall.**

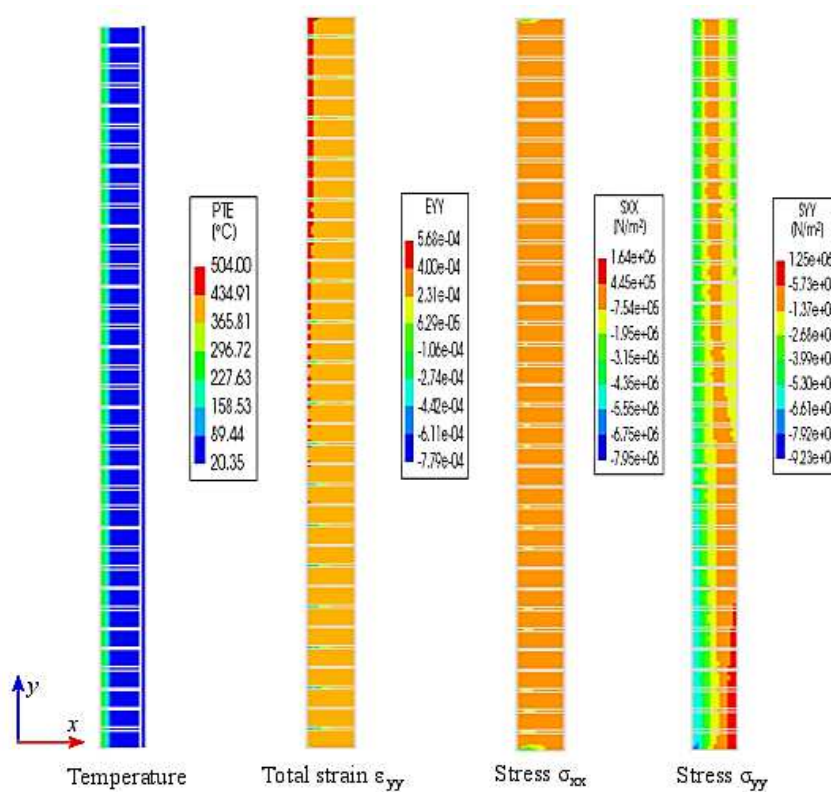
338 It should be mentioned that tensile stresses are considered positive, **whereas** the compressive  
339 stress are considered negative and such **notation** is followed over the entire paper. Firstly, the  
340 results at  $t=5$  min indicate temperature-diffusion across the wall which eventually resulted in  
341 nonlinear thermal gradients across the wall thickness and overall thermal expansion of the wall.  
342 It is to be noted that, in the process of attaining a quasi-static equilibrium, such nonlinear thermal  
343 gradients result in additional stresses in masonry wall which are compressive in the heated zone  
344 and tensile in the adjacent non-heated zone. However, the nature of these stress states are  
345 further influenced by the applied mechanical load and boundary conditions.



346

347 **Figure 10: Deformed configuration of the central line of the half-scale wall (Scaling 30x)**

348 For instance, the presence of a fixed base and a hinged boundary condition at the top of the wall  
 349 under consideration resulted in an additional temperature-induced restraint stresses which are  
 350 compressive in the heated zone and tensile in the non-heated zone. The influence of these  
 351 restraint stresses are evident near the fixed base (see  $\sigma_{yy}$ , Figure 11).



352

353

**Figure 11: Thermo-mechanical response of half-scale masonry wall at t=5 min.**

354

Such a combined stress state resulting from thermal dilation and mechanical boundary conditions

355

resulted in a thermal-bowing profile as shown in Figure 10. Further, no cracking was observed in

356

the wall upto t=5 min. However, after further fire exposure, the thermal diffusion accelerates and

357

the stress states are predominantly influenced by temperature-dependent material degradation in

358

conjunction with cracking and crushing. This can be seen in the thermo-mechanical response at

359

t=23 min (Figure 12), where one can see the predominant tensile zone that induced cracking at

360

the base. Further, such localized cracking significantly influenced the overall mechanical

361

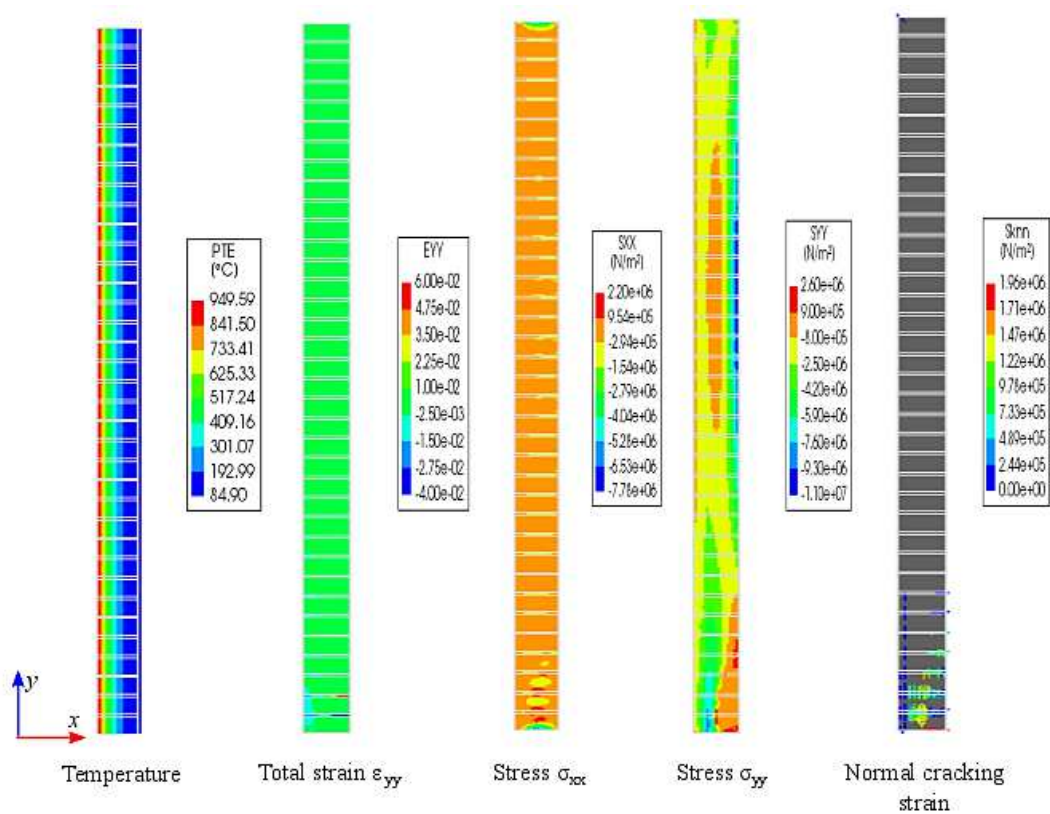
response of the structure and this is explained herein with the aid of thermo-mechanical response

362

histories of representative volume units (RVU) taken at heights of 0.66m (Figure 13 ) and 0 m

363

(Figure 14) from the base, respectively.



364

365

**Figure 12: Thermo-mechanical response of half-scale masonry wall at t=23 min.**

366

Moreover, the stress ( $\sigma_{yy}$ ) histories at the designated locations, labelled as  $M_A$ ,  $M_B$  and  $M_C$  (see

367

Figure 13) in the aforementioned RVUs are shown in Figure 15. During initial stages of fire

368

exposure, in the case of RVU-1, the observed stress states (see Figure 13, t=5 min) are governed

369

by the thermal gradients as well as the fire induced restraint stress due to the fixed base. This

370

resulted in an increase in the compressive stress in the heated zone (Figure 15, RVU-1,  $M_A$ ) and

371

reduction in the compressive stress in the adjacent non-heated zone (Figure 15, RVU-1,  $M_B$ ).

372

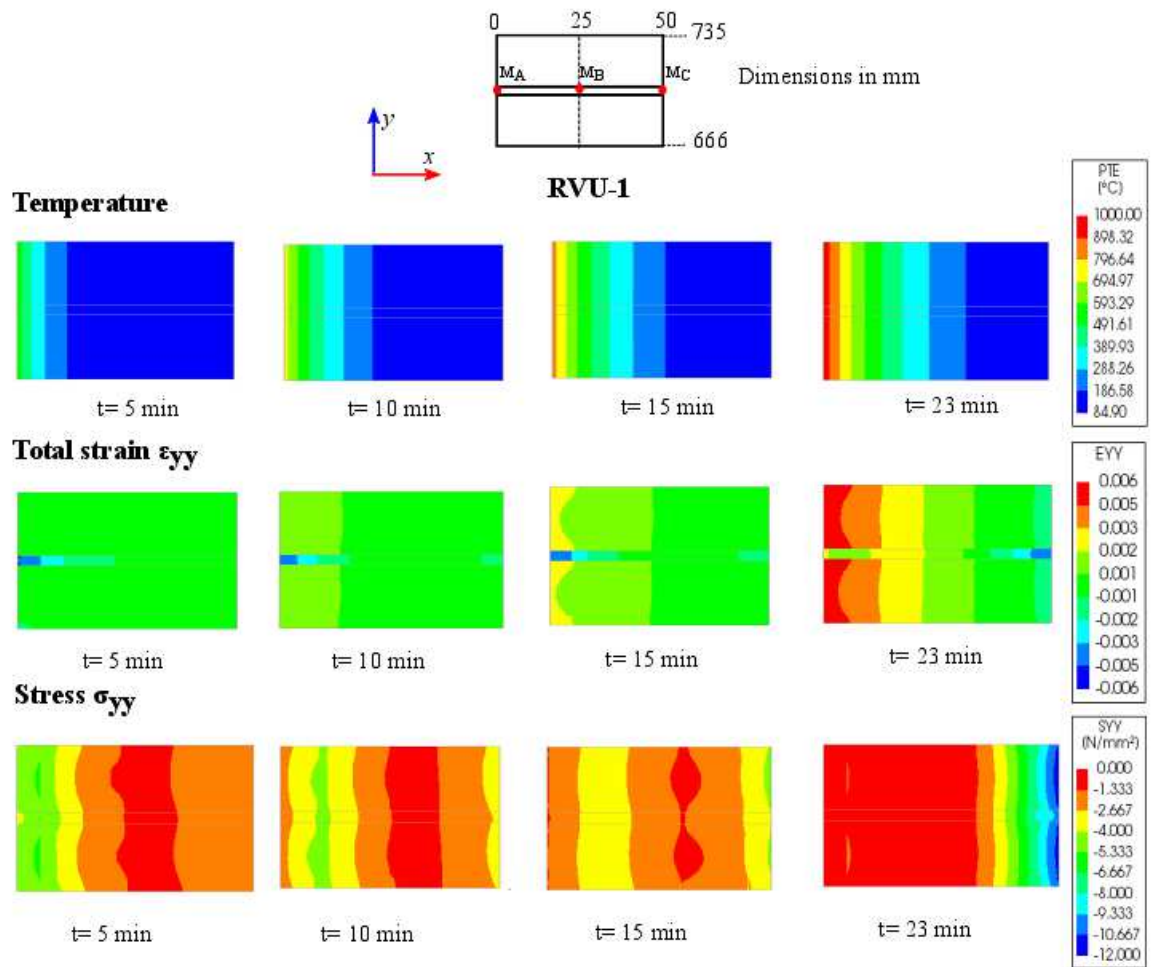
Whereas in the case of RVU-2, an increase in in the compressive stress in the heated zone

373

(Figure 15, RVU-2,  $M_A$ ) and reduction in the compressive stress in the non-heated zone (Figure

374

15, RVU-2,  $M_B$  &  $M_C$ ) are observed.

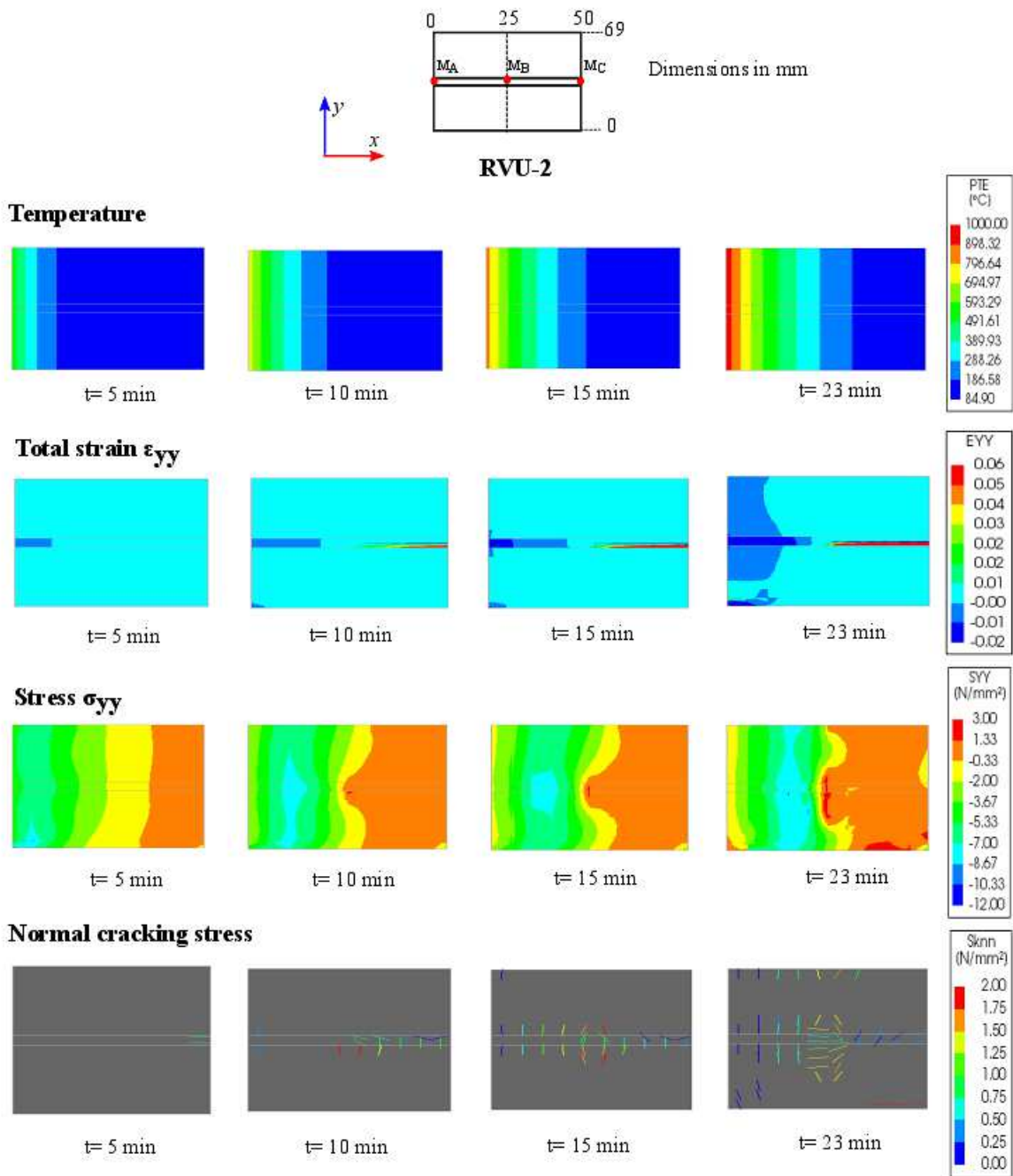


375

376 **Figure 13: Thermo-mechanical response history of RVU-1 (half-scale masonry wall at 0.66**  
 377 **m from base).**

378 However, the increase is higher compared to RVU-1 and is attributed to the predominance of fire  
 379 induced restraint stresses at the base. After further fire exposure, a shift of the compressive zone  
 380 is observed in case of RVU-1 towards the unexposed face (See Figure 13,  $\sigma_{yy}$ ).



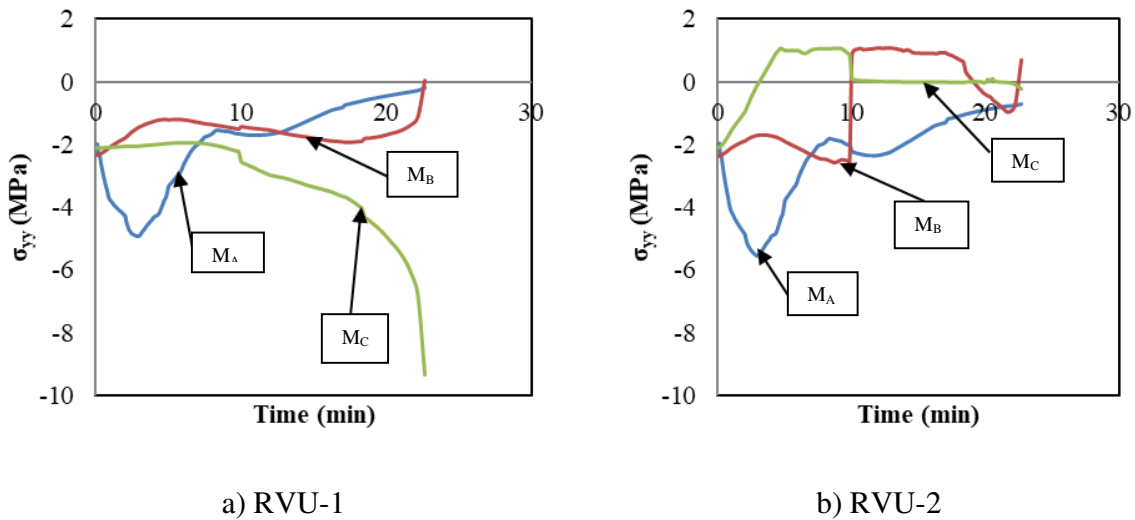


381

382 **Figure 14: Thermo-mechanical response history of RVU-2 (half-scale masonry wall at 0 m**  
 383 **form base).**

384 This is characterized by a reduction in compressive stresses in the heated zone (Figure 15, RVU-  
 385 1,  $M_A$ ) and an increase in compressive stress in the adjacent non-heated zone (Figure 15, RVU-1,

386  $M_B$ ). This is attributed to the temperature-dependent material degradation in the heated zone in  
387 conjunction with the nonlinear thermal gradients arising due to further heat diffusion.



388 **Figure 15: Stress states in RVU-1 and RVU-2 of the half-scale masonry wall.**

389 Whereas in the case of RVU-2, cracking is initiated at the base and an increase in the cracking  
390 zone is observed with further fire exposure (Figure 14, Normal cracking stress). This is  
391 characterized by tensile stress histories in the non-heated zone (Figure 15, RVU-2,  $M_B$  &  $M_C$ ).  
392 Furthermore, in the case of RVU-1, an increase in compressive stress is observed in the non-  
393 heated zone (Figure 15, RVU-1,  $M_C$ ). This is attributed to excessive cracking and crushing at the  
394 base in RVU-2 (Figure 14, Normal cracking stress) and such cracking and crushing releases the  
395 tensile stresses originating from the base. At  $t=23$  min, further cracking is observed in RVU-2  
396 and resulted in the partial release of the rotational restraint at the base. This is characterized by a  
397 change in the stress-states in RVU-1 (Figure 13) and further resulted in the onset of large out of  
398 plane displacements (see Figure 10) and eventually the failure of the masonry wall. However, in  
399 the experimental investigation by Laverty et al. [11,15], on the half-scale masonry wall under  
400 consideration, detailed observations pertaining to the aforementioned cracking induced collapse

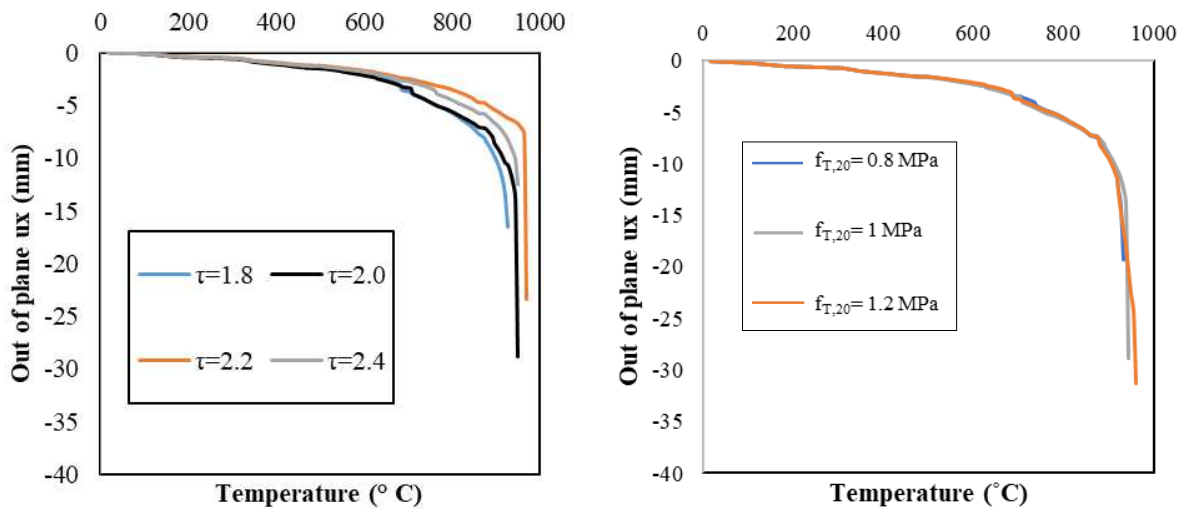
401 were not taken. Laverty et al. [11,15] reported that the fire exposed side of the wall could not be  
402 seen due limitations specifically targeted to their scaled fire test.

### 403 3.3 Parametric studies

404 To quantify the effect of assumed parameters, as well as to demonstrate the accuracy of the  
405 developed FE framework, parametric studies are performed on the half-scale masonry wall.

406 Figure 16a shows the parametric study on transient creep strain, where the coefficient  $\tau$  (See  
407 section 2.3) is varied between 1.8 to 2.4. The results indicate that the increase in  $\tau$  results in  
408 increase in the failure temperature and is due to the reduction in the total thermal strain. Figure

409 16b shows parametric study on the effect of initial tensile strength of mortar ( $f_{t,20}$ ), where the  
410 tensile strength is varied between 0.8 to 1.2 MPa.



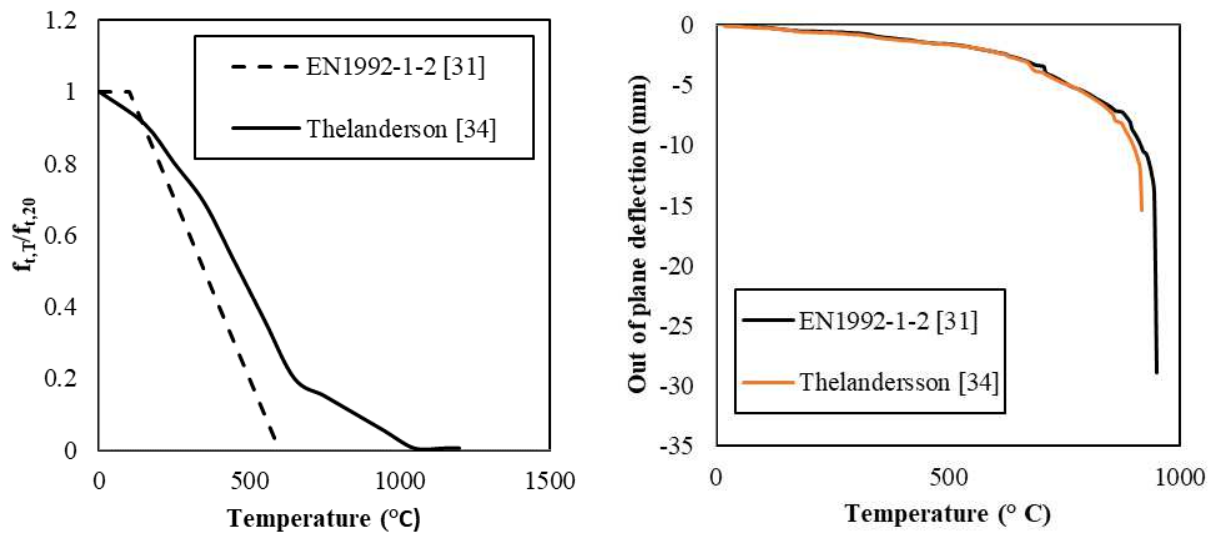
a) Effect of Transient creep

b) Effect of tensile strength of mortar

411 **Figure 16: Parametric studies on transient creep and tensile strength of mortar.**

412 The results indicate slight increase in the failure temperature with increase in the tensile strength  
413 of mortar, with almost similar thermo-mechanical response history. Also, parametric study is

414 performed on the temperature-dependency of the tensile strength of mortar and unit. The  
 415 temperature-dependency as in Thelandersson [34] is compared to that of the EN1992-1-2 [31].  
 416 The thermo-mechanical response histories are observed to be similar in both the cases, with  
 417 slightly higher failure temperature in the case of EN1992-1-2 [31].

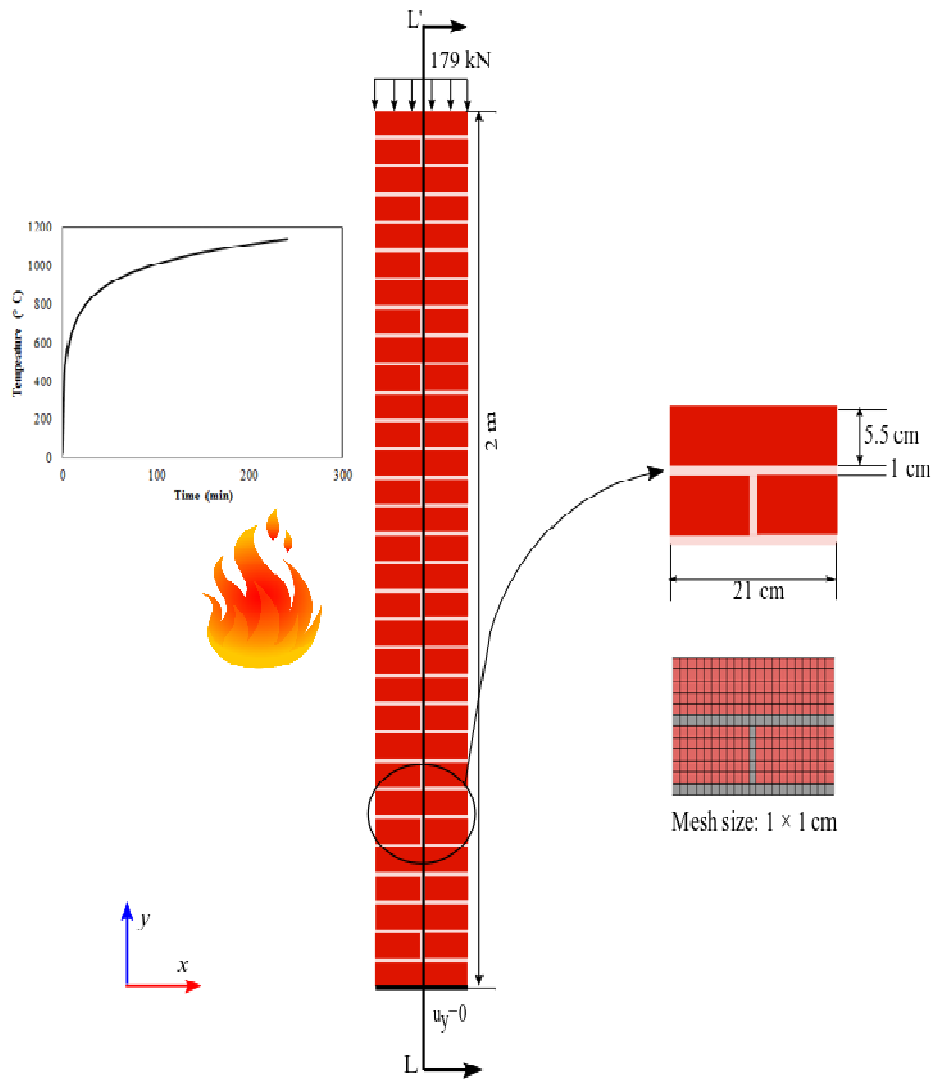


a) Temperature-dependency in tensile strength

b) Effect of temperature-dependency in concrete unit and cement mortar

418 **Figure 17: Parametric studies on temperature-dependency of concrete unit and cement**  
 419 **mortar.**

420 **4 Full-scale masonry wall subjected to ISO-834 fire exposure**



421 s

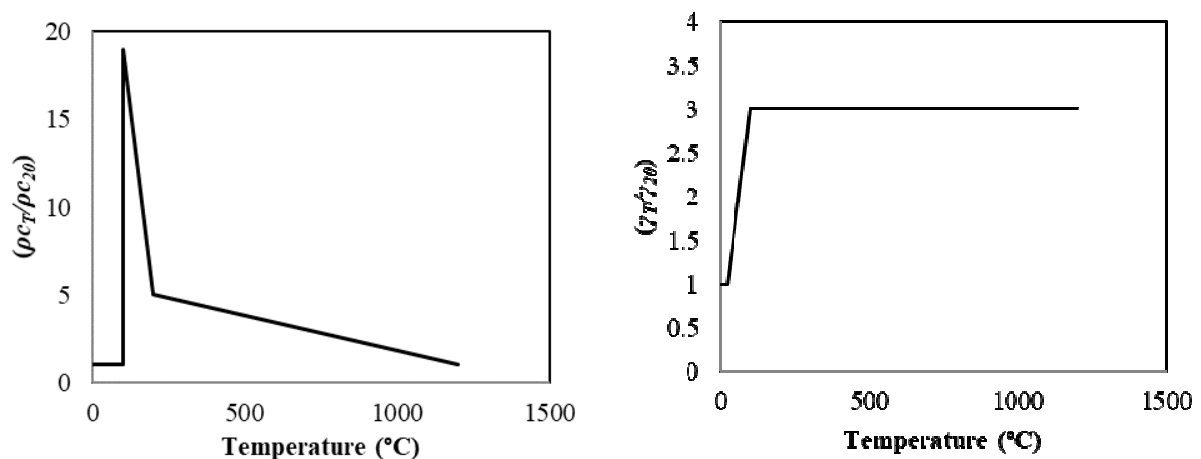
422 **Figure 18: Full-scale masonry wall subjected to standard fire exposure.**

423 Taking advantage of the previously discussed simulation framework, it was decided to study a  
 424 different type of masonry wall. This full-scale wall is made of solid clay bricks and the  
 425 arrangement of the bricks differs from the previous one. This full-scale masonry wall shown in  
 426 Figure 18 is subjected to ISO-834 fire curve, which is also shown in the figure. The wall is  
 427 loaded axially and is fixed at the base, and is free to translate and rotate at the top. The design

428 axial load capacity of the wall is quantified in accordance with the EN1996-1-1 [35] and its  
 429 corresponding fire resistance rating for 50% of the design axial load on the wall is observed to  
 430 be 240 min from the EN1996-1-2. Thermo-mechanical analysis is performed using the 2-D FE  
 431 based simulation framework with the mesh-size shown in Figure 18. As discussed in the case of  
 432 half-scale masonry wall, thermo-elastic analysis is also performed with temperature-dependent  
 433 thermal and mechanical properties. Axial load corresponding to 50% of the load-carrying  
 434 capacity of wall is applied in the form of pressure at the top of the wall, which is 0.853 MPa.

#### 435 4.1 Material properties

436 The material properties utilized for the full-scale masonry wall are presented herein. A summary  
 437 of these properties at room temperature ( $T=20\text{ }^{\circ}\text{C}$ ) is shown in Table 2. In the case of cement  
 438 mortar, the temperature-dependent thermal and mechanical properties are taken from Section 3.1.  
 439 In the case of clay unit, the temperature-dependency in specific heat capacity and thermal  
 440 conductivities of clay unit is taken from the EN1996-1-2 [13] and is shown in Figure 19.

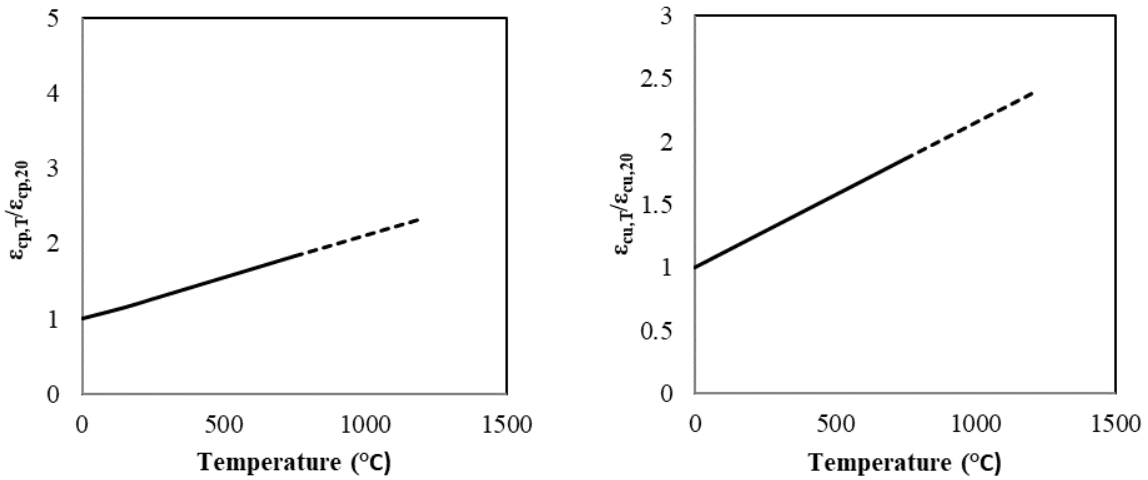


441 a) Specific-heat capacity

b) Thermal-conductivity

**Figure 19: Temperature-dependent thermal properties of clay unit.**

442 Due to the lack of availability of comprehensive studies on the nature of transient creep strain in  
443 clay unit [36] , the transient creep component is ignored in the present numerical simulation. The  
444 temperature-dependent thermal expansion coefficient for the clay unit is taken from the EN1996-  
445 1-2 [13]. The temperature-dependent  $f_{c,T}$ ,  $\varepsilon_{cp,T}$  and  $\varepsilon_{cu,T}$  are taken from EN1996-1-2 [13]. It is to  
446 be noted that the temperature-dependency of above mentioned parameters is shown up to 750 °C  
447 in EN1996-1-2 [13], and for higher temperatures beyond 750 °C, linear extrapolation is followed  
448 in the present study (see Figure 20 and Figure 21). In case of  $f_{t,T}$ , due to the lack of data (both  
449 experimental and code provisions), the temperature-dependency in  $f_{t,T}$  is assumed to be **the**  
450 same as that of  $f_{c,T}$ .

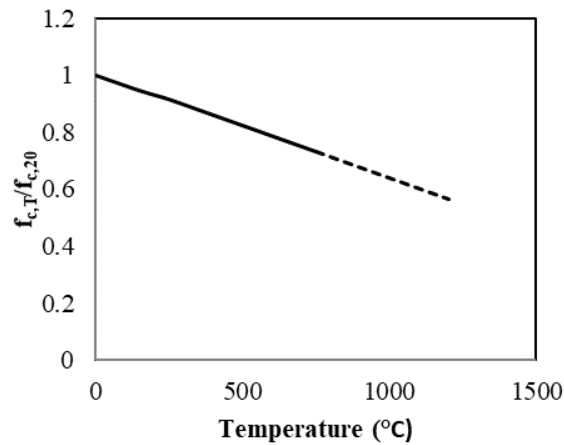


a) Strain at peak compressive strength ( $\varepsilon_{cp,T}$ )

b) Ultimate compressive strain ( $\varepsilon_{cu,T}$ )

451 **Figure 20: Temperature-dependent  $\varepsilon_{cp,T}$  and  $\varepsilon_{cu,T}$  in clay unit.**

452 The mode-1 fracture energy corresponding to room temperature is taken from the work of  
453 Lourenço et al. [37] and to it, the same temperature-dependency as in  $f_{t,T}$  is applied, assuming a  
454 constant ductility index.



455

456

**Figure 21: Temperature-dependent compressive strength of clay unit.**

457

**Table 2: Physical properties of full-scale masonry wall subjected to fire.**

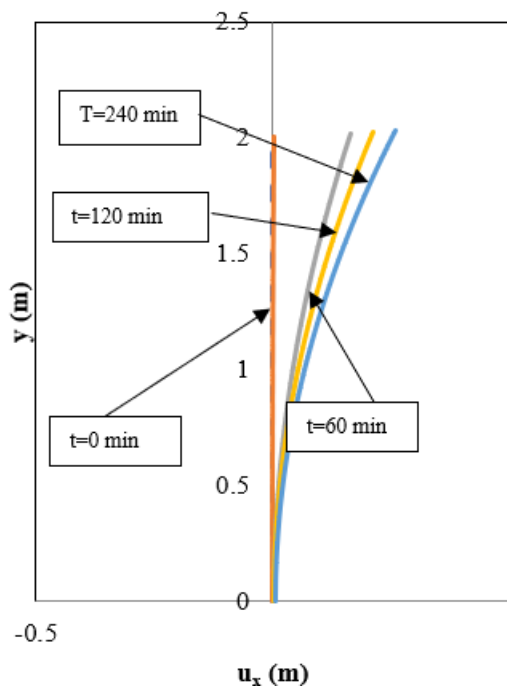
Physical property	Value
Geometry	See Figure 18
Applied load (MPa)	0.8538
<b>Clay unit:</b>	
Compressive strength (MPa)	30
Tensile strength (MPa)	3
Poisson's ratio	0.17
$\epsilon_{cp,20}$	0.00175
$\epsilon_{cu,20}$	0.0019
Thermal expansion coefficient (/°C)	$5.33 \times 10^{-6}$ (Clay units)
Heat capacity (kJ/m <sup>3</sup> K)	676
Thermal Conductivity (W/mK)	0.42
mode-1 fracture energy (N/m)	55
<b>Mortar joint:</b>	
Compressive strength (MPa)	10
Tensile strength (MPa)	1
Poisson's ratio	0.2
$\epsilon_{cp,20}$	0.0025
$\epsilon_{cu,20}$	0.02
Thermal expansion coefficient (/°C)	$6 \times 10^{-6}$ (Calcareous aggregates)
Heat capacity (kJ/m <sup>3</sup> K)	2100
Thermal Conductivity (W/mK)	1.36

458

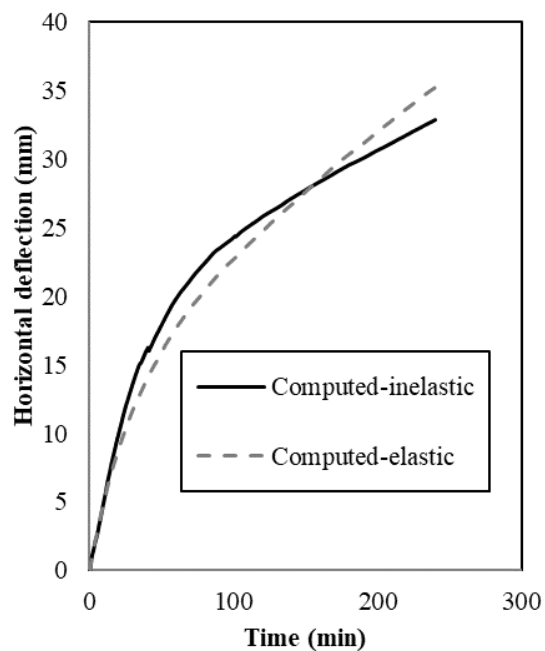


459 **4.2 Results and discussion**

460 The deformed configuration of the central line (scaling 10x) of the wall is shown in Figure 22a.  
461 The deformation history of top of the wall is shown in Figure 22b, for both the elastic and  
462 inelastic cases, respectively. Significant thermal bowing is observed and the rate of increase of  
463 thermal bowing is more predominant in the initial one hour. This is attributed to the nature of the  
464 ISO-834 fire curve coupled with lower thermal conductivities of unit and mortar, which  
465 eventually resulted in higher thermal increments during the initial one hour of fire exposure.  
466 However, no reverse thermal bowing was observed for the masonry wall. It is to be noted that  
467 the deformation histories are similar for both the elastic and inelastic cases, respectively unlike  
468 the half scale wall.



a) Deformed configuration of the central line

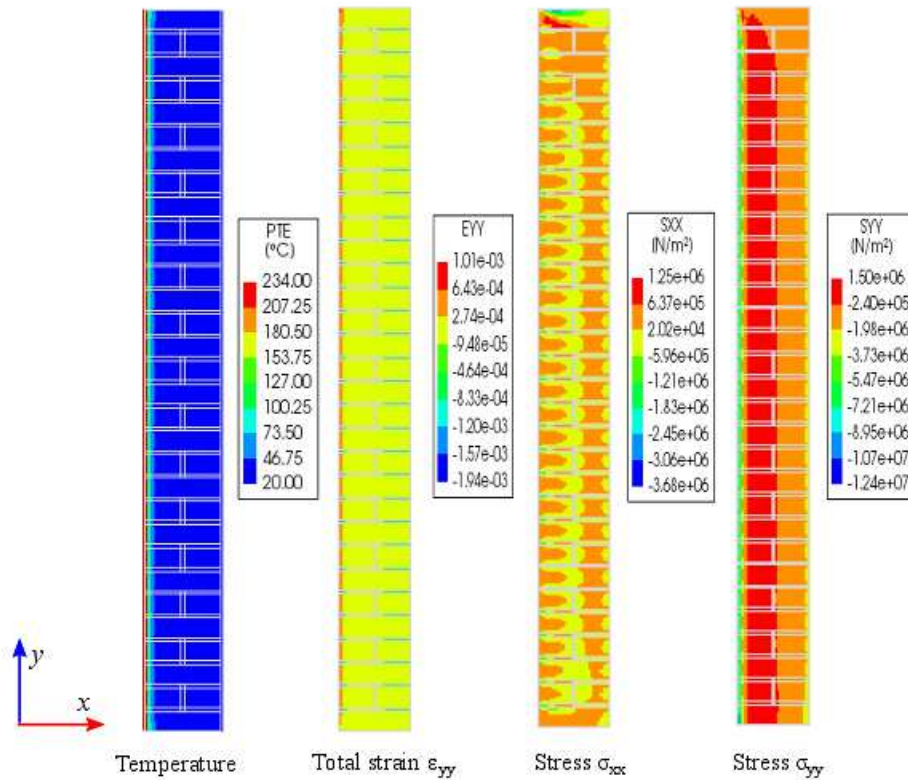


b) Deformation history at the top of the masonry wall

469 **Figure 22: Deformed mechanical response of full-scale wall (Scaling 10x).**

470 However, in the elastic case, higher thermal bowing is observed in comparison to the inelastic  
471 case during the later stages of fire exposure. This is attributed to additional eccentricity due to  
472 the fire induced material cracking. Figure 23 and Figure 24 show the overall thermo-mechanical  
473 response of the masonry walls at t=5 min and t=240 min, respectively. Upon exposure to fire,  
474 highly nonlinear thermal gradients are induced on to the structure and eventually, the presence of  
475 such nonlinear thermal gradients coupled with the mechanical load will result in the overall  
476 thermal expansion of the wall. However, as discussed in the case of half-scale masonry wall  
477 subjected to fire, the thermal expansion in the heated zone results in tension in the adjacent non-  
478 heated zone of the structure and eventually culminate into compressive stress in the heated zone.  
479 This phenomenon can be seen in Figure 23 (t=5 min) where the  $\sigma_{yy}$  at the exposed face is in  
480 compression, whereas the adjacent core to the exposed face is in tension. However, the stress  
481 states in the masonry wall are transient in nature due to nonlinear thermal gradients coupled with  
482 temperature-dependent material degradation and eventually severe cracking is observed in the  
483 wall at t=240 min (Figure 24, Normal cracking stress). The further explanation pertaining to such  
484 thermo-mechanics in the context of the present wall is provided with the aid of RVU-1 (Figure  
485 25) and RVU-2 (Figure 26) taken at 1 m and 0 m heights from the base, respectively. The stress  
486 ( $\sigma_{yy}$ ) histories at the designated locations,  $M_A$ ,  $M_B$  and  $M_C$  (see Figure 23) in the considered  
487 RVUs are shown in Figure 27. In the case of RVU-1, the heated zone is under compression  
488 followed by tension in the adjacent cold zone (Figure 25,  $\sigma_{yy}$  at t=5 min). However, as time  
489 progresses, the aforementioned compression-tension zone transits over the wall thickness (Figure  
490 25,  $\sigma_{yy}$  at t= 60 & 120 min) due to which, cracking is observed in the mortar (Figure 25, Normal  
491 cracking stress) which is relatively weaker compared to the brick units. These effects can be

492 seen in the stress history plots as well (Figure 27, RVU-1,  $M_A$  &  $M_B$ ). Moreover, after further fire  
 493 exposure, a reduction in the compressive stress is observed in the heated zone, whereas reduction  
 494 in tensile stress is observed in the adjacent non-heated zone (Figure 27, RVU-1,  $M_A$  &  $M_B$ ).

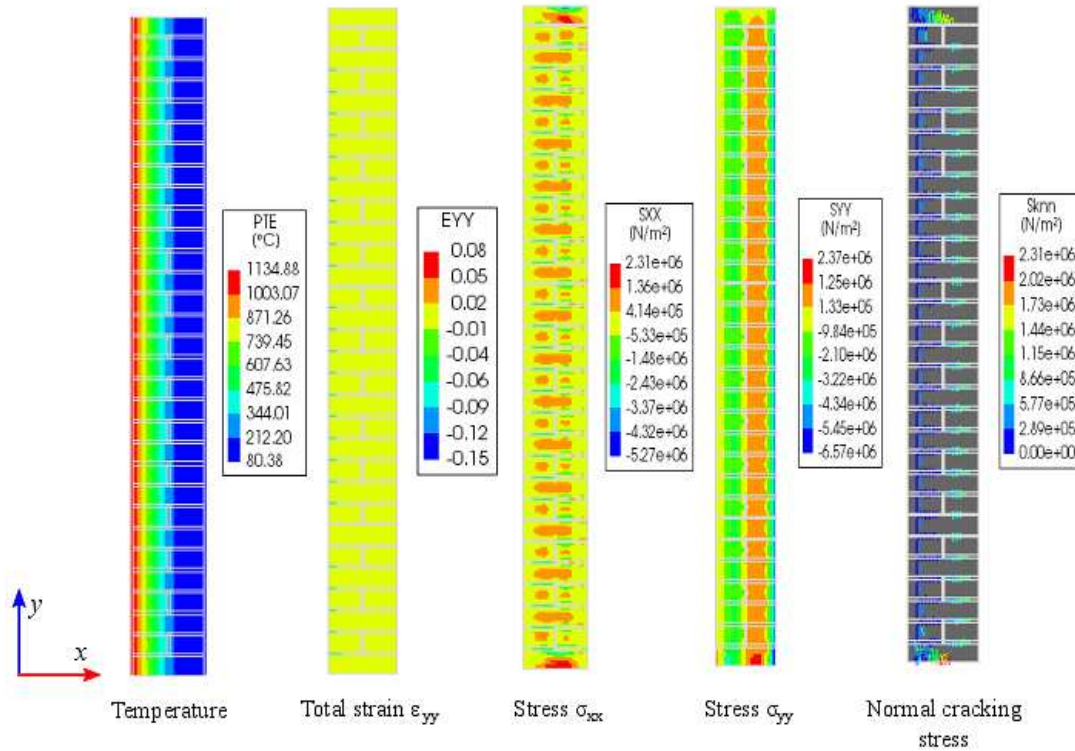


495

496 **Figure 23: Thermo-mechanical response of full-scale masonry wall at t=5 min.**

497 This is mainly due to two thermo-mechanical phenomena. Firstly, change in the nature of  
 498 nonlinear thermal gradients attributed to the cross-sectional heat diffusion. Secondly, due to the  
 499 predominance of the material degradation over thermal dilation in the development of the  
 500 thermal stresses. It should be mentioned that the discontinuity in stress profiles are observed at  
 501 the brick-mortar interface (Figure 25,  $\sigma_{yy}$ ), unlike the earlier half-scale wall due to the additional  
 502 stresses generated due to the differential thermal expansion between the brick and mortar. For

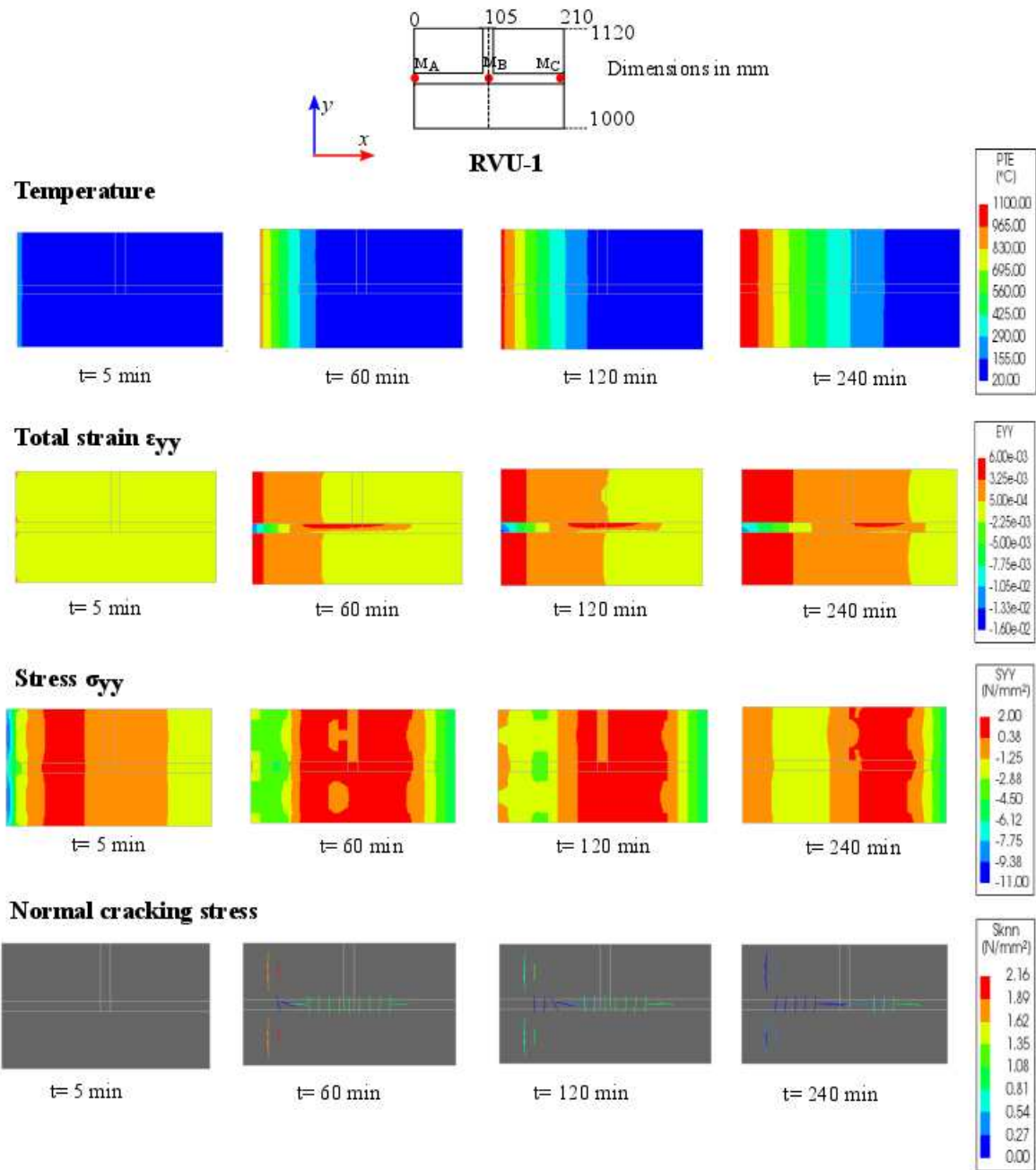
503 instance, for the chosen material properties, thermal increment of 1000 °C attributes to a  
 504 differential thermal strain of 0.00066 which is significant enough to cause additional stresses.



505

506 **Figure 24: Thermo-mechanical response of full-scale masonry wall at t=240 min.**

507 Moreover, such stresses have resulted in vertical cracking (see Figure 25, normal cracking stress  
 508 at t=120 and 240 min) in brick and mortar in the hot and cold zones, respectively. In the case of  
 509 RVU-2 as well, above mentioned thermo-mechanical phenomena were observed with  
 510 quantitatively similar stress (Figure 27, RVU-2) histories to that of RVU-1, with additional  
 511 stresses and cracking zones attributing to the base restraint effects. Lastly, for the full-scale  
 512 masonry wall under consideration, no failure was observed from the numerical simulation, both  
 513 in terms of strength as well as the insulation failure criteria for the 240 min one-sided fire  
 514 exposure.



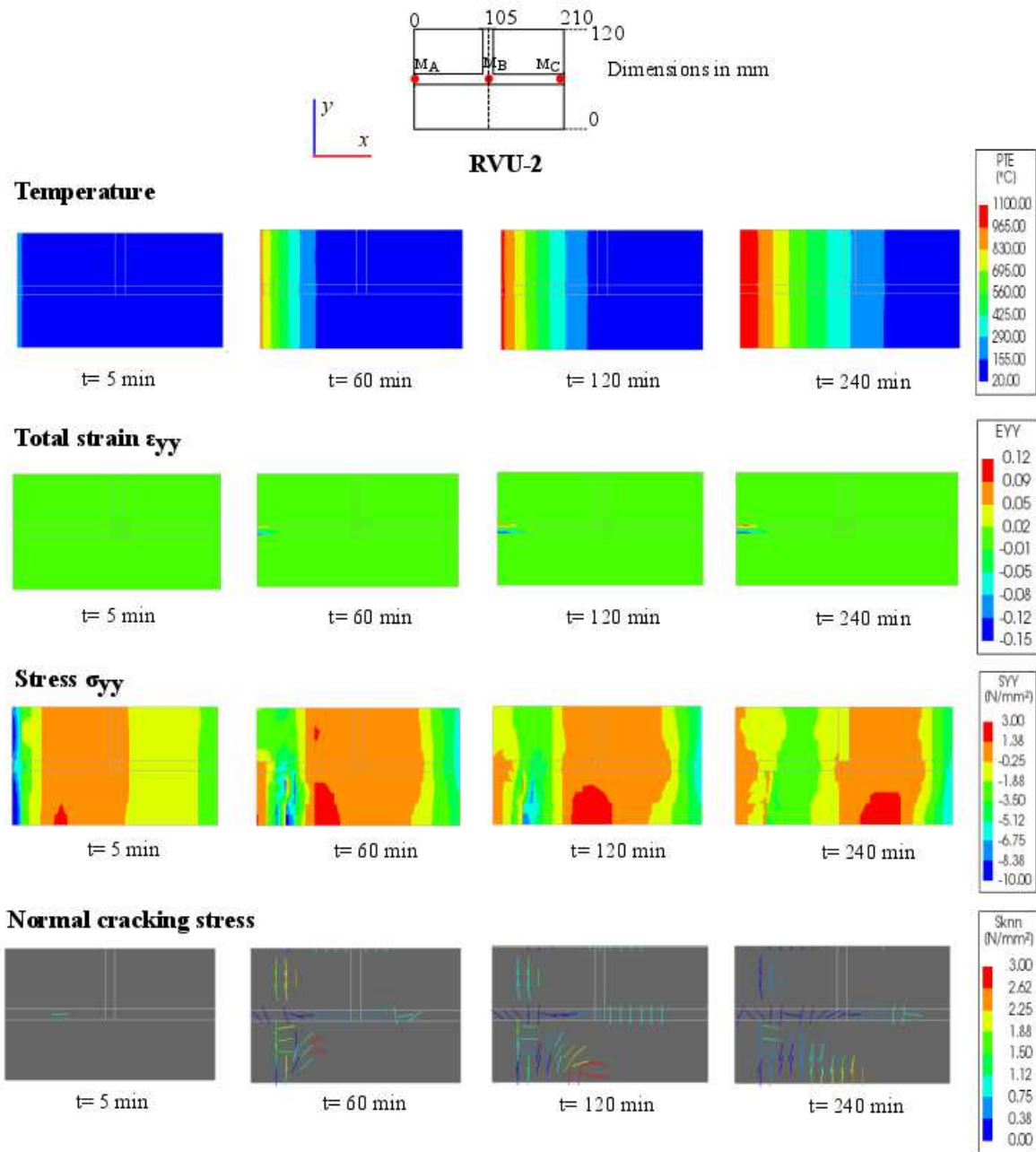
515

516 **Figure 25: Thermo-mechanical response history of RVU-1 (full-scale masonry wall at 1 m**

517

**from base).**

518

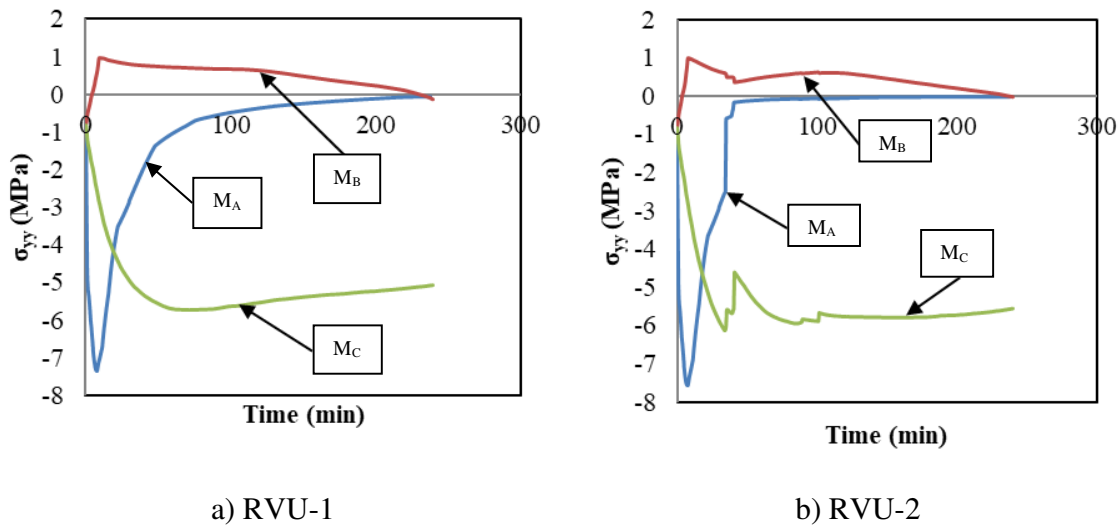


519

520 **Figure 26: Thermo-mechanical response history of RVU-2 (full-scale masonry wall at 0 m**

521

**from base).**



522 **Figure 27: Stress states in RVU-1 and RVU-2 of the full-scale masonry wall.**

523 **5 Conclusions**

524 A 2-D FE based simulation framework has been developed for thermo-mechanical analysis of  
 525 solid brick masonry walls. The developed framework modelled unit and mortar separately, and  
 526 accounted for geometric and material nonlinearities, transient states of strain and temperature-  
 527 dependent material properties. The developed framework was considered validated as the  
 528 thermo-mechanical predictions of half-scale masonry wall subjected to fire and the predictions  
 529 were reasonably accurate, as compared to the experimental results. Utilizing the developed  
 530 framework, thermo-mechanical analysis was performed on a full-scale masonry wall subjected to  
 531 one-sided fire exposure.

532 Critical phenomena which included heat diffusion, nonlinear thermal gradients, unit-mortar  
 533 thermo-mechanical interaction, cracking and stress profiles within the masonry structure were  
 534 studied in detail in the above mentioned numerical investigations. Also, thermo-mechanics  
 535 within a representative volume of unit and mortar at various locations were studied. Such unit



536 level thermo-mechanics studies within the present numerical investigation have indicated the  
537 following insights. In both the walls, influence of boundary conditions was observed on the  
538 stress histories in the representative volume units. In case of the half-scale wall, extensive  
539 cracking and crushing in the masonry wall, especially near the base had resulted in the change in  
540 the kinematic equilibrium of the global structure and eventually culminated to the failure of the  
541 structure. In case of the full-scale clay brick masonry wall, progressive cracking was observed  
542 over time. However, no failure was observed in the numerical simulation for the given fire  
543 exposure, which was taken from the fire resistance ratings tabulated in EN1996-1-2. Moreover,  
544 the differential thermal expansion between the constituent materials of the masonry walls has  
545 resulted in additional stresses at the unit-mortar joint, and eventually resulted in vertical cracking  
546 profiles near the joints. Lastly, the developed 2-D FE simulation framework and subsequent  
547 detailed thermo-mechanical response history characterization demonstrated in the present study  
548 facilitates wide range of numerical applications pertaining to masonry structures. They include a)  
549 performance based structural fire design, b) sensitivity analysis, c) post-fire residual capacity  
550 assessment studies, and d) development of simplified empirical models.

## 551 **6 Acknowledgements**

552 The first author would like to acknowledge the post-doctoral fellowship offered by the  
553 University of Minho for this research. Funding provided by the Portuguese Foundation for  
554 Science and Technology (FCT) to the Research Project IntegraCrete (PTDC/ECM-  
555 EST/1056/2014 - POCI-01-0145-FEDER-016841) is gratefully acknowledged. This work was  
556 financially supported by UID/ECI/04029/2019 - ISISE, funded by national funds through the  
557 FCT/MCTES (PIDDAC).



558 **7 References**

- 559 [1] P.B. Lourenço, G. Milani, A. Tralli, A. Zucchini, Analysis of masonry structures: Review  
560 of and recent trends in homogenization techniques, *Can. J. Civ. Eng.* 34 (2007) 1443–  
561 1457. <https://doi.org/10.1139/L07-097>.
- 562 [2] P.B. Lourenço, Computational strategies for masonry structures: multi-scale modeling,  
563 dynamics, engineering applications and other challenges, in: *Congr. Métodos Numéricos*  
564 *En Ing.*, Semni, Bilbao, 2013: pp. 1–17.
- 565 [3] S. Russo, F. Sciarretta, Masonry exposed to high temperatures: Mechanical behaviour and  
566 properties—An overview, *Fire Saf. J.* 55 (2013) 69–86. [https://doi.org/10.1016/j.firesaf.](https://doi.org/10.1016/j.firesaf.2012.10.001)  
567 2012.10.001.
- 568 [4] European Committee for Standardization, EN 1996-1-2: Design of masonry structures -  
569 Part 1-2: General rules - Structural fire design, 2006.
- 570 [5] American Concrete Institute, ACI 216.1-07 / TMS-0216-07: Code Requirements for  
571 Determining Fire Resistance of Concrete and Masonry Construction Assemblies, 2007.
- 572 [6] M. Dhanasekaran, V. Chandrasekaran, S. Grubits, A numerical model for thermal bowing  
573 of masonry walls, in: *10th Int. Brick/Block Mason. Conf.*, Calgary, 1994.
- 574 [7] A. Nadjai, M. O'Garra, F.A. Ali, D.L.-F. and materials, undefined 2003, A numerical  
575 model for the behaviour of masonry under elevated temperatures, *Wiley Online Libr.*  
576 (n.d.). <https://onlinelibrary.wiley.com/doi/abs/10.1002/fam.824> (accessed March 15,  
577 2019).
- 578 [8] S.M. Byrne, Fire resistance of load-bearing masonry walls, *Fire Technol.* 15 (1979) 180–

- 579 188. <https://doi.org/10.1007/BF01983196>.
- 580 [9] S. Lawrence, N. Gnanakrishnan, The fire resistance of masonry walls-an overview, in:  
581 Natl. Struct. Eng. Conf., National conference publication (Institution of Engineers,  
582 Australia), Melbourne, 1987: pp. 431–437.
- 583 [10] T. Shields, D. O’Connor, G.W.H. Silcock, H.A. Donegan, Thermal bowing of a model  
584 brickwork panel, in: Int. Brick/Block Mason. Conf., Dublin, 1988: pp. 846–856.
- 585 [11] D. Lavery, A. Nadjai, D.J. O’connor, Modelling of thermo-structural response of concrete  
586 masonry walls subjected to fire, J. Appl. Fire Sci. 10 (2000) 3–19.
- 587 [12] T.-D. Nguyen, F. Meftah, Behavior of clay hollow-brick masonry walls during fire. Part 1:  
588 Experimental analysis, Fire Saf. J. 52 (2012) 55–64. <https://doi.org/10.1016/J.F>  
589 IRESAF.2012.06.001.
- 590 [13] EN1996-1-2: Design of masonry structures. Part 1–2: General rules –Structural Fire  
591 Design. Commission of European Communities, Brussels, 2005.
- 592 [14] Beureu of Indian Standards, “Indian Code of Practice for fire safety of buildings(General):  
593 Details of Construction-Code of Practice.,” IS-1641, New Delhi, 1989.
- 594 [15] A. Nadjai, M. O’Garra, F. A. Ali, D. Lavery, A numerical model for the behaviour of  
595 masonry under elevated temperatures, Fire Mater. 27 (2003) 163–182.
- 596 [16] A. Nadjai, M. O’Garra, F. Ali, Finite element modelling of compartment masonry walls in  
597 fire, Comput. Struct. 81 (2003) 1923–1930. <https://doi.org/10.1016/S0045->  
598 7949(03)00212-8.

- 599 [17] A. Nadjai, M. O’Gara, F. Ali, R. Jurgen, Compartment Masonry Walls in Fire Situations,  
600 Fire Technol. 42 (2006) 211–231. <https://doi.org/10.1007/s10694-006-7509-6>.
- 601 [18] T.-D. Nguyen, F. Meftah, Behavior of hollow clay brick masonry walls during fire. Part 2:  
602 3D finite element modeling and spalling assessment, Fire Saf. J. 66 (2014) 35–45.  
603 <https://doi.org/10.1016/J.FIRESAF.2013.08.017>.
- 604 [19] P. Kumar, G. Srivastava, Effect of fire on in-plane and out-of-plane behavior of reinforced  
605 concrete frames with and without masonry infills, Constr. Build. Mater. 167 (2018) 82–  
606 95. <https://doi.org/10.1016/J.CONBUILDMAT.2018.01.116>.
- 607 [20] DIANA, DIANA User’s Manual Release 10.2, (2019).
- 608 [21] A. Mohyeddin-Kermani, Modelling and performance of RC frames with masonry infill  
609 under in-plane and out-of-plane loading, The University of Melbourne, 2011.
- 610 [22] Naus D J, The Effect of Elevated Temperature on Concrete Materials and Structures - A  
611 Literature Review, Oak Ridge National Laboratory, Oak Ridge, 2005.
- 612 [23] J. Argyris, J. Doltsinis, On the natural formulation and analysis of large deformation  
613 coupled thermomechanical problems, Comput. Methods Appl. Mech. Eng. 25 (1981) 195–  
614 253.
- 615 [24] R.D. Cook, D.S. Malkus, M.E. Plesha, R.J. Witt, Concepts and applications of finite  
616 element analysis, John Wiley & Sons, Newyork, 2007.
- 617 [25] G. Torelli, P. Mandal, M. Gillie, V.-X. Tran, Concrete strains under transient thermal  
618 conditions: A state-of-the-art review, Eng. Struct. 127 (2016) 172–188.  
619 <https://doi.org/10.1016/J.ENGSTRUCT.2016.08.021>.

- 620 [26] G. Srivastava, P.R. Prakash, An integrated framework for nonlinear analysis of plane  
621 frames exposed to fire using the direct stiffness method, *Comput. Struct.* 190 (2017) 173–  
622 185.
- 623 [27] Y. Anderberg, S. Thelandersson, Stress and deformation characteristics of concrete at high  
624 temperatures. Experimental investigation and material behaviour model, Lund Institute of  
625 Technology, Lund University, Sweden, 1976.
- 626 [28] R. Cope, P. Rao, L. Clark, P. Norris, Modeling of reinforced concrete behavior for finite  
627 element analysis of bridge slabs, in: *Numer. Methods Non-Linear Probl.*, Pineridge Press,  
628 Swansea, 1980: pp. 457–470.
- 629 [29] J.G. Rots, Various crack concepts for curved fracture in concrete, in: *Proc. 7th Int. Conf.*  
630 *Fract.*, Elsevier Ltd, Houston, 1989: pp. 2279–2287.
- 631 [30] H. Akbar, Cracking in reinforced concrete analysis, *J. Struct. Eng. (United States)*. 110  
632 (1984) 1735–1746. [https://doi.org/10.1061/\(ASCE\)0733-9445\(1984\)110:8\(1735\)](https://doi.org/10.1061/(ASCE)0733-9445(1984)110:8(1735)).
- 633 [31] European Committee for Standardization, EN 1992-1-2: Design of concrete structures -  
634 Part 1-2: General rules - Structural fire design, 2004.
- 635 [32] M. Crisfield, *Non-linear finite element analysis of solids and structures.*, 1st ed., Wiley,  
636 Newyork, 1993.
- 637 [33] International Fedaration for Structural Concrete, *FIB Model Code for Concrete Structures*,  
638 Ernst & Sohn, 2010.
- 639 [34] S. Thelandersson, *Effect of High Temperatures on Tensile Strength of Concrete*, Lund  
640 Institute of Technology, 1972.

- 641 [35] European Committee for Standardization, EN 1996-1-1: Design of masonry structures -  
642 Part 1-1: General rules for reinforced and unreinforced masonry structures, 2005.
- 643 [36] J. Brooks, Concrete and Masonry Movements, Elsevier, 2015.
- 644 [37] P.B. Lourenço, J. Almeida, J. Barros, Experimental investigation of bricks under uniaxial  
645 tensile testing, Mason. Int. 18 (2005) 11–20.
- 646